INSTITUT POLYTECHNIQUE DE PARIS

Thèse de Master

école normale supérieure paris–saclay

ÉCOLE POLYTECHNIQUE

IP PARIS

Performance Evaluation of Wireless Capacitor Charging with Cockcroft-Walton Multiplier

Thèse de Master de l'Institut Polytechnique de Paris
préparée à l'Ecole polytechnique

Thèse présentée et soutenue à Palaiseau, le 06 septembre 2024, par

YIMING WEI

Morgan Almanza

Professor, École normale supérieure Paris-Saclay — Directeur de thèse

Acknowledgements

First and foremost, I would like to express my deepest gratitude to Prof. Morgan Almanza for giving me the opportunity to work on this master thesis project and for letting me join SATiE laboratory. Your patient guidance has been a tremendous source of motivation for me. Over the course of these five months of internship, I have learned so much. During our weekly meetings, you provided us with ample opportunities for enriching discussions and imparted invaluable knowledge in power electronics design. From circuit design and component selection to PCB layout, SMT soldering, and the use of various measurement instruments during experiments, you have been there every step of the way, teaching us with hands-on dedication. Without your help, I would have found it nearly impossible to design my first PCB and ensure its proper functioning.

Moreover, you have constantly helped us integrate into the SATiE community. You encouraged us to participate in the monthly SATiE seminars, the 2024 Congrès Junior Pluridisciplinaire, and the SATiE annual meeting, which allowed us to connect with a wider audience. The informal chats during coffee breaks made us feel truly part of the team. Additionally, your attention to our career development, along with the times you brought us croissants and hosted us at your home, made us feel your genuine care and support.

For me, it has been an extraordinary privilege to be your student. You have consistently pointed out areas in the project that needed attention, helped me structure my thesis, patiently answered my questions, and personally assisted in troubleshooting experimental challenges. Thanks to you, I had the chance to design my first PCB, for which I am profoundly grateful!

I would also like to extend my heartfelt thanks to Guojun Lan and Christophe Baron. We shared many insightful discussions, conducted experiments together, and enjoyed a wonderful time. This experience has not only provided me with valuable PCB design knowledge but has also left me with cherished memories that I will carry with me throughout my life.

Contents

List of Figures

List of Tables

Chapter 1

Introduction

Heart Failure (HF) is a chronic, progressive condition where the heart is unable to pump sufficient blood to meet the metabolic demands of the body. It represents the terminal phase of various cardiovascular diseases, including coronary artery disease, hypertension, and cardiomyopathy. Globally, HF affects approximately 75 million people from Fig. 1.1, with a prevalence that continues to rise due to an aging population and improved survival rates following acute cardiac events. In Europe, it is estimated that 15 million people are living with heart failure, and the prevalence continues to rise due to an aging population and improved survival rates following acute cardiac events [1]. The burden of HF is profound, both in terms of mortality and healthcare costs. HF is responsible for substantial cardiovascular mortality across Europe, with a five-year survival rate post-diagnosis of less than 50%. Additionally, the economic impact is substantial, with HF-related healthcare costs estimated to be over €29 billion annually in Europe [1].

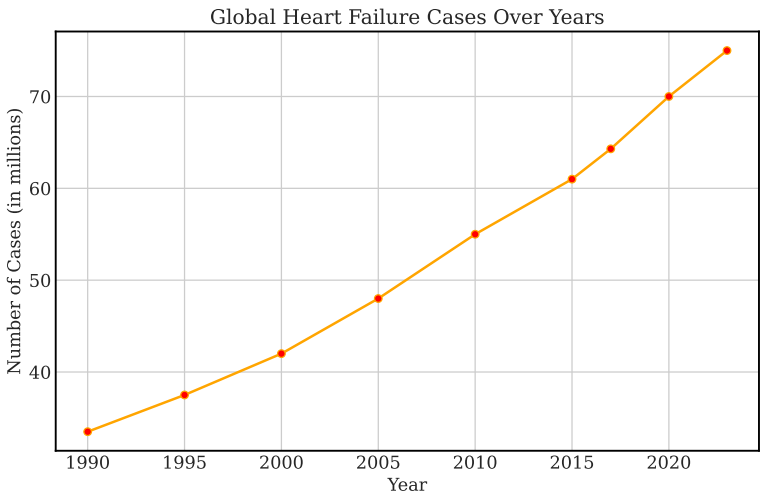

Figure 1.1: Global Heart Failure Cases Over Years. Data source comes from [2, 3].

1.1 Artificial Assist Devices

To manage HF, various mechanical circulatory support devices have been developed, primarily Ventricular Assist Devices (VADs) and Intra-Aortic Balloon Pumps (IABP) see Fig. 1.2. VADs are mechanical pumps that assist the ventricles in pumping blood, used as both a bridge to heart transplantation and as a destination therapy. They have proven effective in improving survival and quality of life for patients with advanced HF. However, they are associated with complications such as infection, bleeding, and thrombosis [4].

IABPs, on the other hand, work by inflating and deflating a balloon within the aorta, thereby reducing cardiac workload and improving coronary blood flow. While IABPs are widely used for short-term support in acute HF settings, their efficacy in chronic management is limited and they carry risks such as vascular injury and thrombosis [5]. Also, due to their pneumatic drive mechanism, IABP devices are typically bulky and challenging to fully implant [6].

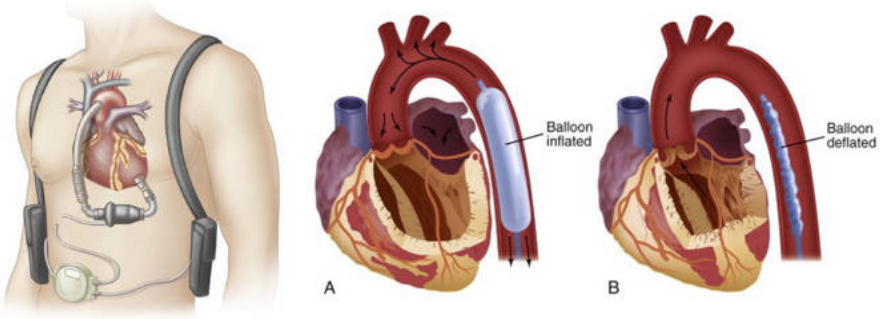

Figure 1.2: Two typical artificial assist devices: (Left) VAD (Right) IABP. Images from Internet.

1.1.1 Dielectric Elastomer Augmented Aorta

Given the limitations of current mechanical support devices, there is a continuous need for innovative solutions. Dielectric elastomer actuators (DEAs) are a class of soft actuators consisting of hyper-elastic membranes sandwiched between compliant electrodes [7]. When an electric field is applied, the membrane compresses out-of-plane and expands in-plane due to the generated Maxwell stress see Fig. 1.3. Key characteristics of DEAs include their ability to undergo large deformation, with strains capable of exceeding 100%, their fast response times which enable quick actuation, and their lightweight design which makes them particularly suitable for medical implants.

Due to these characteristics, this smart material has been utilized in various advanced applications such as valveless impedance-driven pumping [8], flexible robotics [9], and artificial muscles. Notable examples include the artificial urinary sphincter [10], actuator neuroprosthesis for facial paralysis [11, 12], and the dielectric elastomer augmented aorta [6].

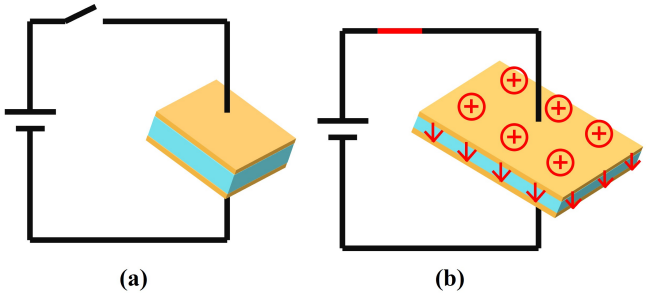

Figure 1.3: Operating principle of DEA: it compress itself while high voltage applied.

Morgan Almanza et *al.* present the first dielectric-elastomer augmented aorta (DEAA) [6]. The DEAA is designed to assist the heart by replacing a segment of the aorta with a tubular DEA, see Fig. 1.4 (d). This innovative device functions through an aortic counter-pulsation approach: during systole, voltage at 7 kV is applied to soften the DEAA, allowing it to expand as the ventricle ejects blood, thus reducing the afterload on the heart. At the beginning of diastole, the voltage is removed, causing the DEAA to contract and augment forward blood flow, mimicking the natural Windkessel effect of the aorta.

The DEAA offers several advantages: it provides efficient energy transfer, contributing about 5-10% of the heart's energy and reducing the workload on the left ventricle. Unlike bulky pneumatic devices, the electrically driven DEAA can be fully implanted. Additionally, the materials used in the DEAA are biocompatible, reducing the risk of adverse reactions [6, 13–15]. The controlled stiffness of the DEA material optimizes assistance during different phases of the cardiac cycle without requiring additional complex elements for pre-stretching.

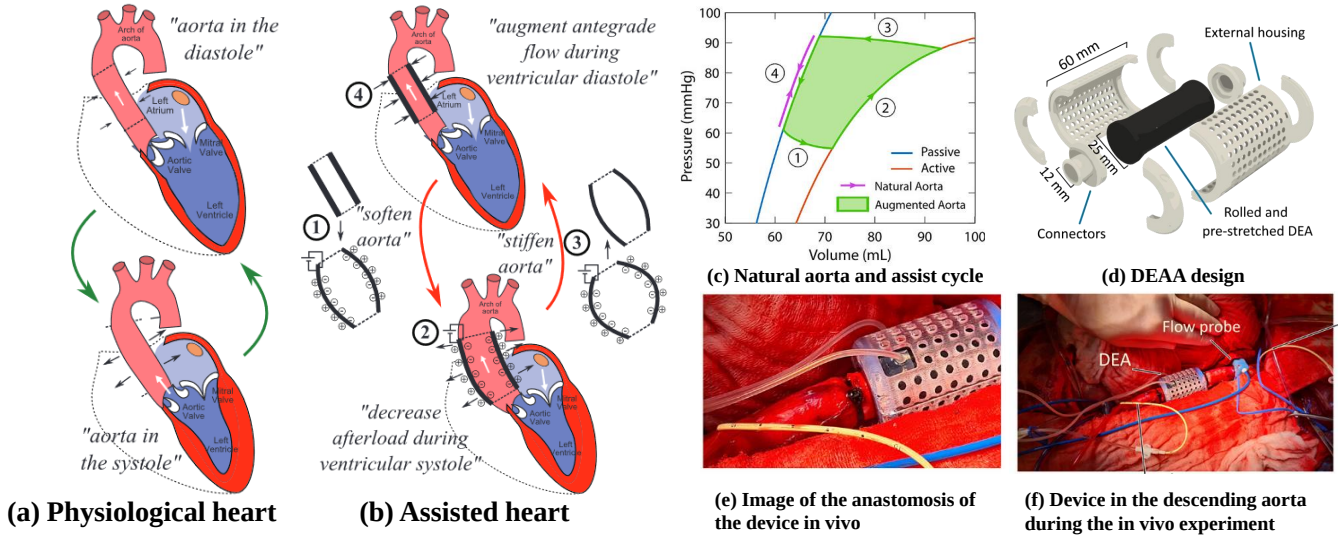

Figure 1.4: (a) Physiological behavior of the heart. (b) Cycle of the DEAA. (c) The pressure–volume characteristics of the DEA in its passive (blue) and active (orange) states, compared to the natural aorta (purple). By alternating its compliance through activation and deactivation, the DEA supplies energy to the cardiovascular system, indicated by the green area. (d) Schematic of the DEA design. (e) Image of the anastomosis of the device in vivo. (f) Image of the implantation DEAA in the descending aorta during the in vivo experiment. Reprinted from [6, 13–15].

1.1.2 Power Supply of DEAA

Due to the unique properties of DEA materials, powering them requires very high voltages (kV) and small currents (mA). Traditional methods like half-bridge (H-bridge), flyback, and multilevel converters have been employed. H-bridge and bidirectional flyback converters using 4.5 kV stacked MOSFETs can achieve up to 16 kV and 7.5 kV, respectively [16, 17]. However, for low-power devices, parasitic capacitance losses drastically reduce efficiency to around 15%. Additionally, the inductors in these designs can be bulky, up to 20 times the volume of the DEA, and stacked MOSFETs increase overall volume. Flyback converters, while useful, produce sharp and pulsatile currents, unsuitable for DEAs needing nearly constant current. Improving the current profile with filtering capacitance further increases volume and energy requirements, making H-bridge and flyback converters less suitable for compact and efficient DEA designs.

Due to that, a solid-state Marx modulator (S^2M^2) is adapted to supply a low-power (120 mW), high-voltage DEA, achieving an overall efficiency of 88% and a voltage up to 12.5 kV [18]. As shown in Fig. 1.5 (a), The S^2M^2 system is composed of N levels, each containing a capacitor (C_k), a diode (D_k), and two MOSFETs (high-side HS_k and low-side LS_k). When LS_k are on and HS_k are off, capacitors are connected in parallel, and in the opposite configuration, they are connected in series. During parallel connection, capacitors charge through the diodes and current source generator connected to V_1. In series connection, a high voltage is achieved, and energy is limited but recharged cyclically through the DEA's operation.

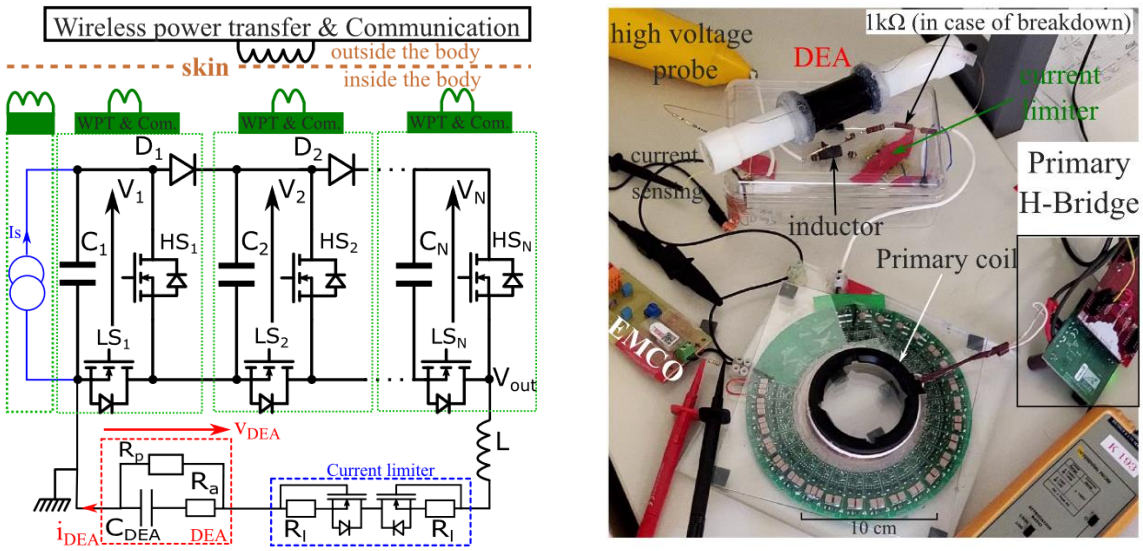

(a) Modified solid-state Marx generator **(b) Image of Adapted Marx modulator**

Figure 1.5: Overview of Adapted Solid-State Marx Modulator. Reprinted from [18].

The cardiac assist cycle consists of four stages over a period of 1 second as shown in Fig. 1.6:

1. **Diastole (0.5s)**: DEA stays at zero voltage, LS_k on, HS_k off, capacitors recharge.

2. **Fast Charge (50ms)**: LS_k turn off sequentially, HS_k turn on in steps, charging capacitors in series.

3. **Systole (0.5s)**: DEA maintains high voltage, HS_k stay on, energy transfer from capacitors keeps voltage drop minimal.

4. **Fast Discharge (50ms)**: HS_k turn off sequentially, LS_k turn on in steps, discharging capacitors in series.

This approach minimizes inrush current and Joule losses, achieving a higher efficiency by splitting the voltage change into smaller steps and recovering energy during discharge.

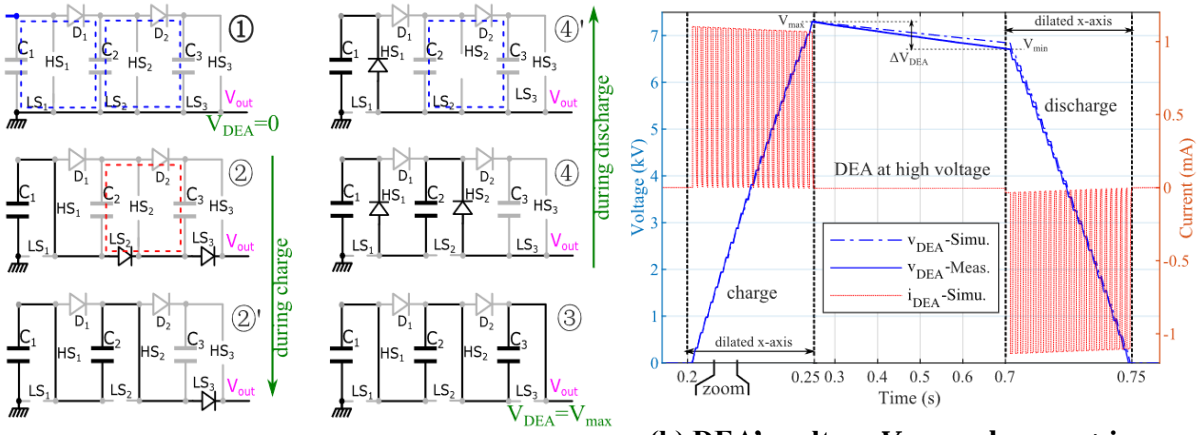

(a) Evolution of the structure

(b) DEA's voltage V_{DEA} and current i_{DEA} along a cycle.

Figure 1.6: Operating principle of S^2M^2. Reprinted from [18].

As shown in Fig. 1.5, a compact but unregulated DC-HVDC converter (A06P-5 from EMCO) supplies the energy for the first level (charging the capacitors C_k in parallel at $V_1 \approx 320$ V, then capacitors C_k are changed in series to arrive 7.5 kV). However, the EMCO converter's design is not sufficiently compact for implanted medical device, presenting challenges in integration and efficiency.

This thesis aims to design a new structure to replace the EMCO converter, focusing on achieving a more compact, efficient, and wireless power transfer for DEAA.

1.1.3 Wireless Power Transfer for Medeical Devices

With the advancement of Gallium Nitride (GaN) devices, achieving higher switching frequencies has become possible, paving the way for more efficient wireless power transfer systems. Wireless power transfer (WPT) has already found widespread application in consumer electronics, such as smartphones, where it provides a convenient and cable-free charging solution [19]. In the realm of transportation, electric vehicles (EVs) and high-speed trains have also adopted WPT technologies to enhance convenience and reduce dependence on traditional charging infrastructure [20, 21]. These applications demonstrate the robustness and efficiency of wireless power systems.

The need for wireless power transfer extends significantly into the medical field, particularly for implantable medical devices. Traditional implantable devices require percutaneous drivelines to receive power, as shown in Fig. 1.7 (a), which are prone to infections at the exit site due to mechanical trauma, tension, and bacterial overgrowth. Studies have shown that driveline infections are a major cause of morbidity and mortality among patients using implantable medical devices, such as Left Ventricular Assist Devices (LVADs) [22]. For instance, driveline infections remain a critical issue, with infection rates reaching up to 25% within two years of implantation [23].

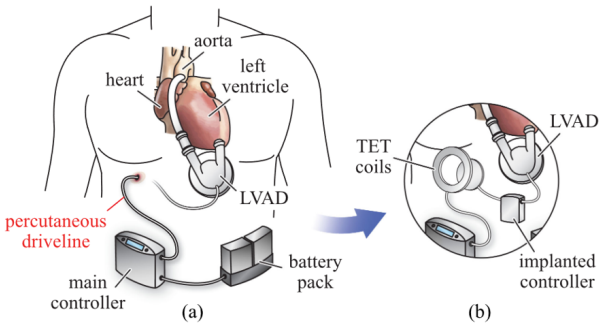

Figure 1.7: Mechanical circulatory support (MCS) system as it is used today. (b) Fully implantable MCS system, with a WPT system. Reprinted from [24].

Based on that, the Zurich Heart project in Switzerland, has developed an innovative wireless power transmission system for Left Ventricular Assist Devices (LVADs) [25], as shown in Fig. 1.8 . This system utilizes WPT approach to wirelessly transfer up to 30W of power across the skin at 800 kHz with an output voltage of 35V, with an efficiency greater than 95% [26]. Safety measures include an electric shielding layer to mitigate internal electric fields, reducing the maximum internal electric field strength from 224V/m to 77V/m and the Specific Absorption Rate (SAR) from 1.21W/kg to 0.25W/kg [27]. In addition to LVADs, WPT systems are being developed for other implantable medical devices such as cardiac pacemakers [28] and miniaturized, and large-scale neural interfaces [29] by providing a reliable and infection-free power source, enhancing overall functionality and patient comfort. However, WPT systems that require high voltage output have not been extensively studied. This is precisely what we need to address.

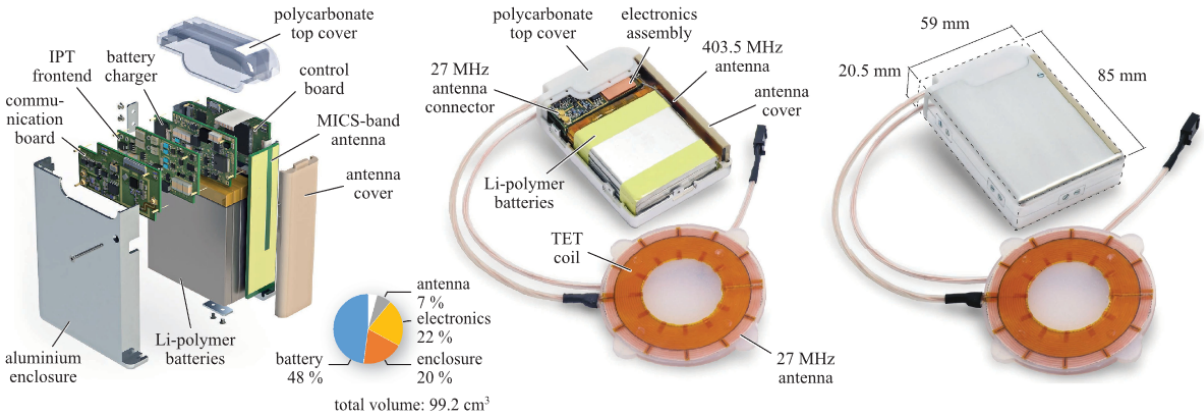

Figure 1.8: Image of the WPT implant prototype. Reprinted from [24].

1.2 Goals and Contributions of the Thesis

The objective of this thesis is to design and optimize a WPT system capable of charging the capacitors in a Marx Modulator. This involves replacing the wired EMCO boost structure [30] shown in Fig. 1.9 (d) yellow block with a wireless transfer system that provides a DC output voltage of over 330V. Additionally, the WPT system must comply with safety regulations concerning tissue heating and human exposure to electromagnetic fields. Although numerous WPT systems have been developed in the past, there has been no demonstration of a WPT system that requires high DC voltage and low power. Therefore, this thesis investigates various wireless power transfer circuit topologies and explores multiple high voltage output schemes, providing a comparative evaluation of each.

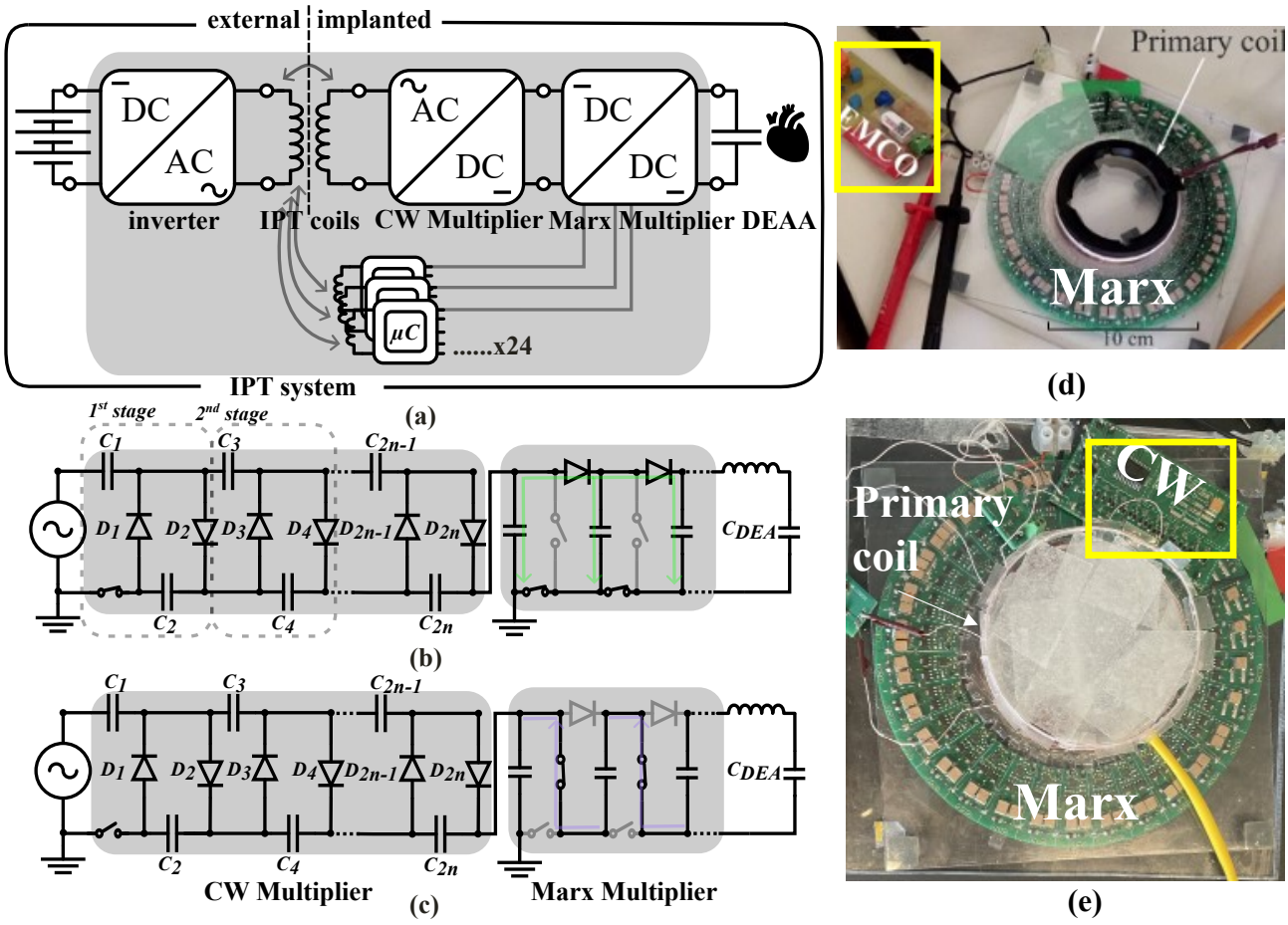

Figure 1.9: (a-c) Schematic concept of the improved DEAA power supply. (d) Initial DEAA power supply. Reprinted from [18]. (e) Improved DEAA power supply.

Through detailed analysis and design, the Cockcroft-Walton Voltage Multiplier (CW) is chosen as the rectifier circuit for the WPT system in Fig. 1.9 (a). This configuration can complete the charging of the Marx capacitors within 0.5 seconds in Fig. 1.9 (b) , after which the CW multiplier stops charging and the Marx modulator begins to operate. This results in the capacitors being reconfigured in parallel, ultimately achieving a high voltage output of 7.5 kV to supply the DEAA in Fig. 1.9 (c).

1.3 Outline of the Thesis

As discussed earlier, designing a low-power system capable of periodically charging capacitors with high voltage involves addressing several engineering challenges. This thesis is divided into three chapters, each focusing on resolving different aspects of the system.

Chapter 2: In this chapter, we begin by introducing the coupling model of the receiving coil in a WPT system, specifically focusing on the mutual inductance between coils. We then explain the necessity of using compensation capacitors for impedance matching and introduce four classic compensation topologies (SS, SP, PS, PP), discussing their respective characteristics. To achieve high-voltage charging of the load capacitors, we discuss several potential approaches, such as direct capacitor charging using constant current output from SS compensation or increasing the receiver coil size to enhance the output voltage. However, these solutions do not adequately address the safety and size constraints for implantable DEAA devices, leading us to the next chapter.

Chapter 3: This chapter focuses on the rectification of the WPT output. We introduce the Cockcroft-Walton (CW) rectifier circuit, which effectively steps up a small AC input to a high-voltage DC output, addressing the issues identified in the previous chapter. We discuss the circuit's principles, the dynamics of voltage multiplication, and the equivalent output circuit. A CW circuit designed to convert a 15V AC input into a 360V DC output is presented, along with an analysis of its efficiency.

Chapter 4: In this chapter, we firstly explore the LCC-S compensation topology, which is more robust against variations in coupling coefficients. Then we combine the WPT system with the CW rectifier circuit, analyzing the characteristics of their integration. We propose an equivalent input circuit for the CW in this context, providing a simpler method for analysis, and conduct a Fourier Harmonic Analysis (FHA) of the circuit. Finally, we evaluate the overall efficiency, safety, and size of the combined system.

Chapter 5: The final chapter summarizes the designed circuits and the proposed equivalent analysis methods. It also outlines potential areas for optimization and suggests directions for future design improvements.

Chapter 2

Wireless Power Transfer System

James Clerk Maxwell laid the foundation for wireless energy transmission with his electromagnetic wave theory in 1865 [31]. Later, Nikola Tesla built on this theory by inventing the Tesla coil, aiming to achieve wireless power transfer [32]. Although Tesla's ambitious plans were never fully realized, his pioneering ideas inspired future developments in the field [33]. In the late 20th century, advancements in Gallium Nitride (GaN) semiconductor technology and litz wire enabled higher frequency operations, making wireless power transfer more feasible. These higher frequencies made it easier to transfer energy via electromagnetic waves, rekindling interest in wireless power technologies among engineers [33].

This resurgence was notably marked by MIT's groundbreaking work on Wireless Power Transfer via Strongly Coupled Magnetic Resonances [34]. Since then, extensive research has been conducted, exploring applications ranging from wireless charging of vehicles [20] and drones [35] to powering smartphones [19] and medical implants [36, 37] in Fig. 2.1. This method has significantly enhanced the freedom and convenience of powering devices and transmitting information [38] by eliminating the constraints of physical wiring.

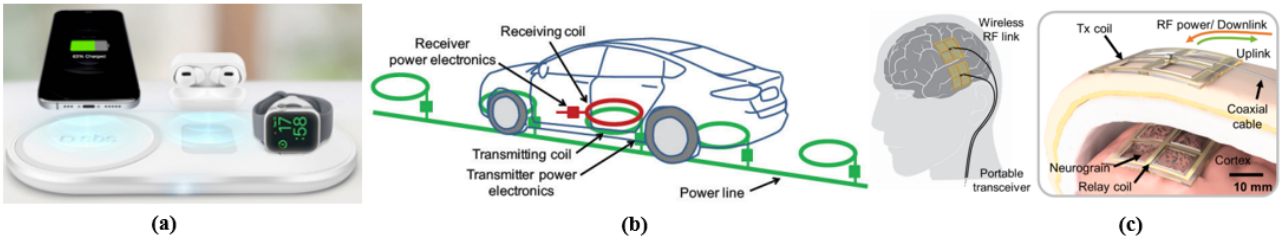

(a) (b) (c)

Figure 2.1: (a) Qi charging pad. (b) E-Mobility for electric vehicles.Reprinted from [39]. (c) Wireless Neural Interface. Reprinted from [40].

2.1 WPT Fundamentals

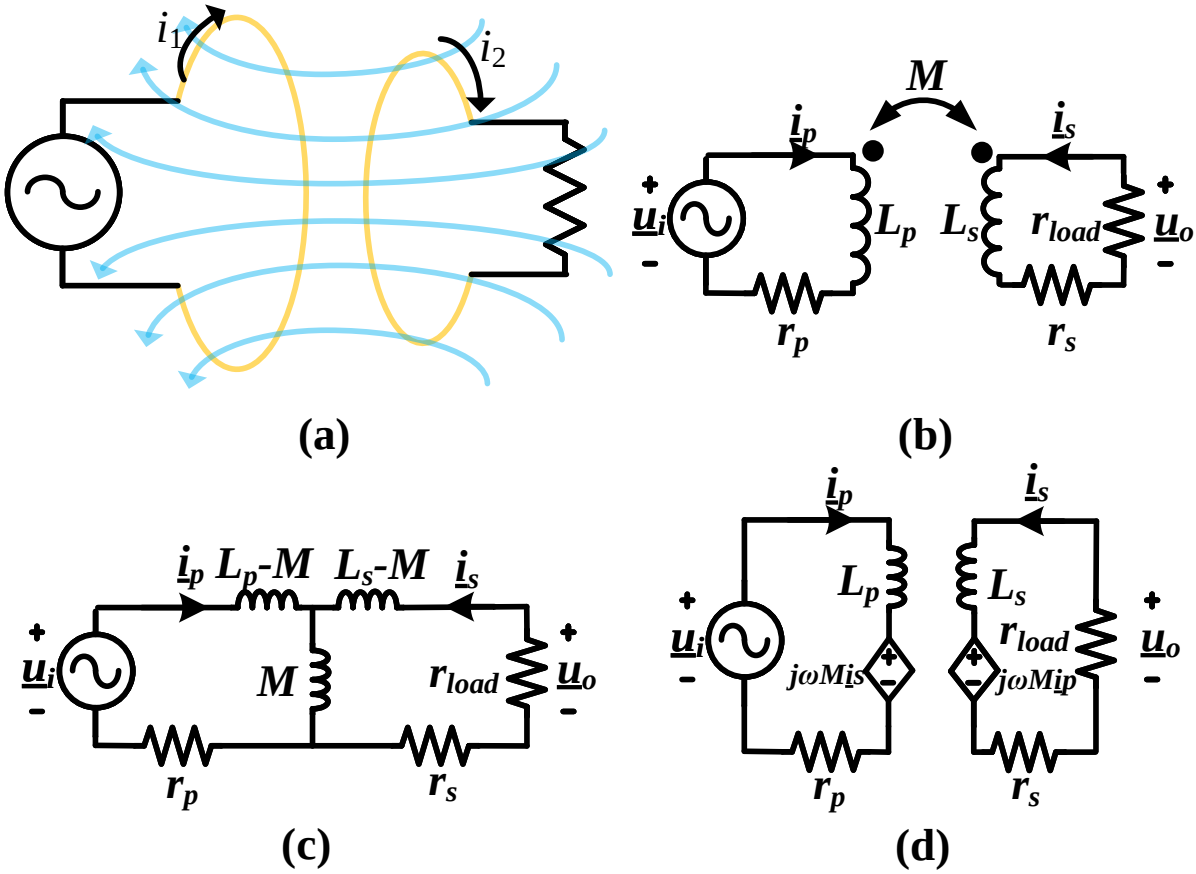

Figure 2.2: (a) Schematic of two magnetically loosely coupled coils. (b) its electrical circuit model. (c) T-type transformer equivalent circuit. (d) General two-port transformer equivalent circuit.

Wireless power transfer operates similarly to a transformer, but with loose coupling, as shown in Fig.2.2 (a). The system involves two coils, L_p and L_s, which exhibit inductive properties. These coils are separated by a certain distance and are linked by mutual inductance M. When an AC voltage is applied to L_p, a current is induced in the distant coil L_s, allowing energy to be transferred wirelessly. The coupling coefficient k is defined as in a traditional transformer and is given by

$$k = \frac{M}{\sqrt{L_p L_s}} \in [0, 1], \tag{2.1}$$

where k represents the degree of coupling between the coils.

Since for mutually coupled coils, the self- and the mutual inductance act always simultaneously, the circuit in Fig. 2.2 (b) is mathematically described with

$$\begin{bmatrix} \underline{u}_i \\ \underline{u}_o \end{bmatrix} = j\omega \cdot \begin{bmatrix} L_p & M \\ M & L_s \end{bmatrix} \cdot \begin{bmatrix} \underline{i}_p \\ \underline{i}_s \end{bmatrix}, \tag{2.2}$$

where $\underline{u}_i$ and $\underline{u}_o$ are the phasor voltages across the respective coils, $\underline{i}_p$ and $\underline{i}_s$ are the phasor currents through the coils, and ω is the angular frequency. In this analysis, the internal resistances r_p and r_s of the coils L_p and L_s are neglected. According to Equ. 2.2, we can have T-type transformer equivalent circuit in Fig. 2.2 (c) and general two-port transformer equivalent circuit in Fig. 2.2 (d).

The current phasor $\underline{i}$ can be derived from Fig. 2.2 (d) as

$$\underline{i}_p = \frac{\underline{u}_i - j\omega M \underline{i}_s}{j\omega L_p}, \quad \underline{i}_s = \frac{-j\omega M \underline{i}_p}{r_{load} + j\omega L_s}. \tag{2.3}$$

and $\underline{u}_o$ on load resistance is:

$$\underline{u}_o = \frac{j\omega M \underline{i}_p r_{load}}{r_{load} + j\omega L_s}. \tag{2.4}$$

That means for a given primary current $\underline{i}_s$, it produces a loss of $\underline{i}_p^2 r_p$ in the primary winding and induces a voltage with the RMS value of $\omega M \underline{i}_p$ in the secondary winding. This induced voltage is applied to the impedance $r_{load} + j\omega L_s$ on the secondary side, so the induced current and voltage are largely restricted by the reactance of the secondary winding. The same situation is for the primary side. If the reactance of the secondary side impedance could be compensated, for example, by connecting a capacitor C_s in series with the secondary winding and canceling out the reactance as shown in Equ. 2.3, we will have:

$$\underline{u}_i = j\omega_r M \underline{i}_s, \quad \underline{i}_s = \frac{-j\omega_r M \underline{i}_p}{r_{load}}, \quad \underline{u}_o = j\omega_r M \underline{i}_p. \tag{2.5}$$

in the condition of:

$$j\omega_r L_s + \frac{1}{j\omega_r C_s} = 0 \quad j\omega_r L_p + \frac{1}{j\omega_r C_p} = 0$$

then a larger load current and a higher load power can be transferred to the load. With the same input voltage in the primary side, the output power is increased and volt-ampere (VA) rating is decreased thereby, the power transfer capability and efficiency are improved. The final circuit looks like Fig. 2.3 (c), with two capacitors series in two sides, it is called series-series (SS) compensation.

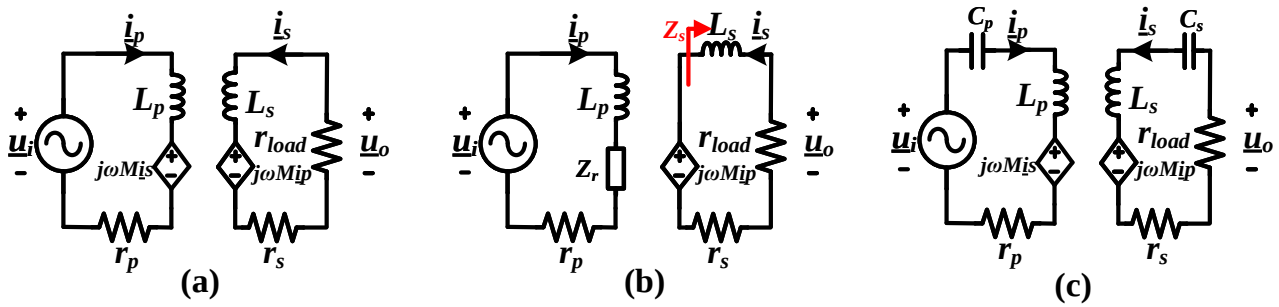

Figure 2.3: WPT circuit without/with series-series compensation.

2.1.1 Reflected Impedance

In general two-port transformer equivalent circuit as shown in Fig. 2.3 (a), the current controlled voltage source in primary side could be considered as a impedance with the help of Z_s the impedance seen from the current controlled voltage source in secondary side:

$$\underline{Z}_s = \frac{j\omega M\underline{i}_p}{-\underline{i}_s} = j\omega L_s + r_{load} + r_s. \tag{2.6}$$

$$\underline{Z}_r = \frac{j\omega M\underline{i}_s}{\underline{i}_p} = \frac{j\omega M j\omega M}{-\underline{Z}_s} = \frac{\omega^2 M^2}{\underline{Z}_s} \tag{2.7}$$

in the case of SS compensation, the reactive part is compensated by capacitor, so we will have pure resistive reflected load:

$$\underline{Z}_r = \frac{\omega^2 M^2}{r_{load} + r_s} \tag{2.8}$$

We could find the the bigger r_{load} is, the smaller $\underline{Z}_r$ will be. Also if we have a inductive load like Equ. 2.6, we will have a capacitive load for $\underline{Z}_r$ and vice versa, the proof is below.

$$\underline{Z}_r = \frac{\omega^2 M^2}{j\omega L_s + r_{load} + r_s} = \frac{\omega^2 M^2 (r_{load} + r_s - j\omega L_s)}{(r_{load} + r_s + j\omega L_s)(r_{load} + r_s - j\omega L_s)} = \frac{\omega^2 M^2 (r_{load} + r_s - j\omega L_s)}{(r_{load} + r_s)^2 + \omega^2 L_s^2} \tag{2.9}$$

2.1.2 Load-independent Current (LIC) and Load-independent Voltage (LIV) Output

When using WPT technology, the load is typically variable. For example, when charging a lithium battery, as illustrated in Fig. 2.4, a constant current source is usually required at the beginning. During the constant current (CC) charging period, the battery voltage rises from near zero to its maximum value. As the load voltage increases and reaches a threshold, the charging mode switches to a constant voltage source, during which the battery current drops from the rated value to near zero [41–44]. During this period, according to Ohm's law, the battery can be modeled as a

variable resistor with a wide range of values [44, 45]. For such a variable load, we generally expect a voltage source or current source that is independent of the load.

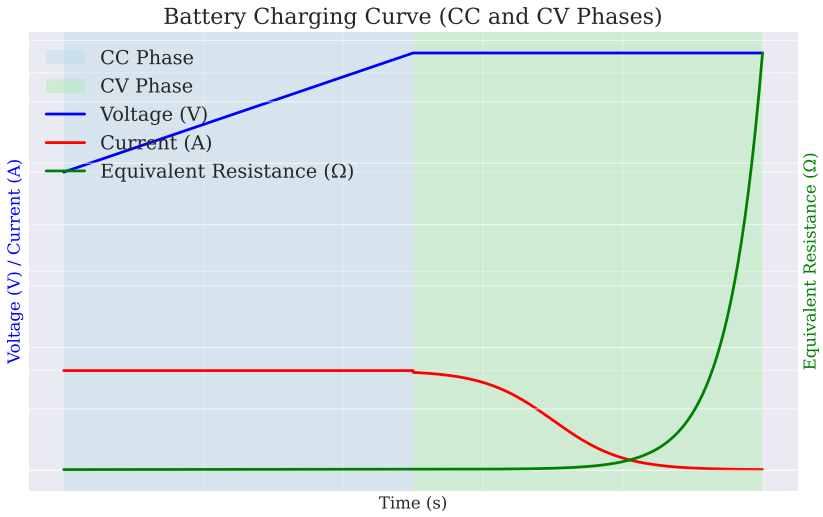

Figure 2.4: Typical CC/CV charging profile of the Li-ion battery.

In SS compensation, we could have inherently CC or CV output features by setting input source with special frequency under condition of ignoring coil internal resistance. As illustrated before, the input voltage source $\underline{u}_i$ have a angular frequency ω_r, we series connect two capacitors C_p, C_s on either side with value in Fig. 2.5 (a):

$$j\omega_r L_s + \frac{1}{j\omega_r C_s} = 0, \quad j\omega_r L_p + \frac{1}{j\omega_r C_p} = 0.$$

at this time, L_p, L_s are resonating respectively with C_p, C_s, which could be considered as short circuit as shown in Fig. 2.5 (b), then the $\underline{u}_i$ is fix and will clamp the current controlled voltage source $j\omega_r M\underline{i}_s$, which means $\underline{i}_s = \frac{\underline{u}_i}{j\omega_r M}$, a current source seen by the load in the secondary side.

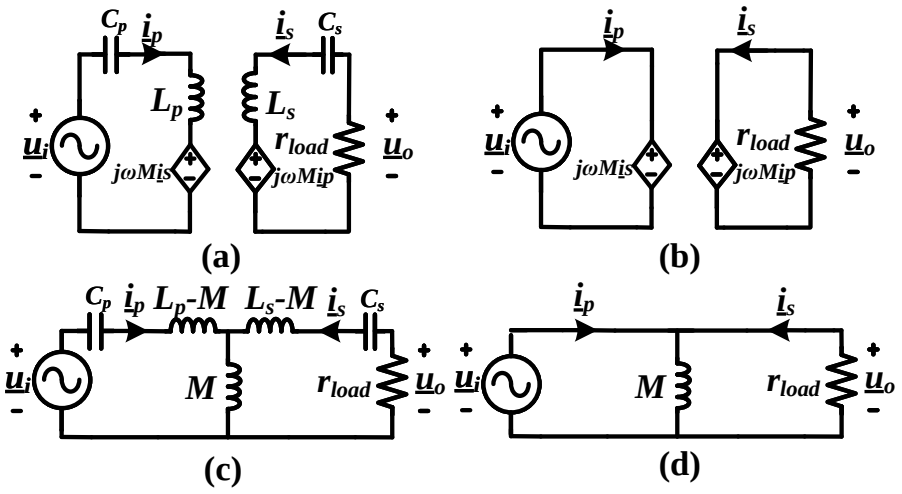

Figure 2.5: (a-b) SS Constant Current output behaviour. (c-d) SS-Constant Voltage output behaviour.

With the same C_p, C_s value, but the $\underline{u}_i$ is fed with angular frequency ω_H which satisfies as shown in Fig. 2.5 (c), C_p, C_s resonating respectively with $L_p - M, L_s - M$, which could be considered as short circuit in Fig. 2.5 (d), then the voltage source $\underline{u}_i$ is directly put on load - load independent voltage characteristic is fulfilled.

$$\omega_H = \frac{1}{\sqrt{(L_p - M)C_p}} = \frac{1}{\sqrt{(L_s - M)C_s}}, \tag{2.10}$$

with Equ. 2.1 we could further get:

$$\omega_H = \frac{\omega_r}{\sqrt{1-k}}, \quad \frac{|\underline{u}_o|}{|\underline{u}_i|} = \sqrt{\frac{L_s}{L_p}} \tag{2.11}$$

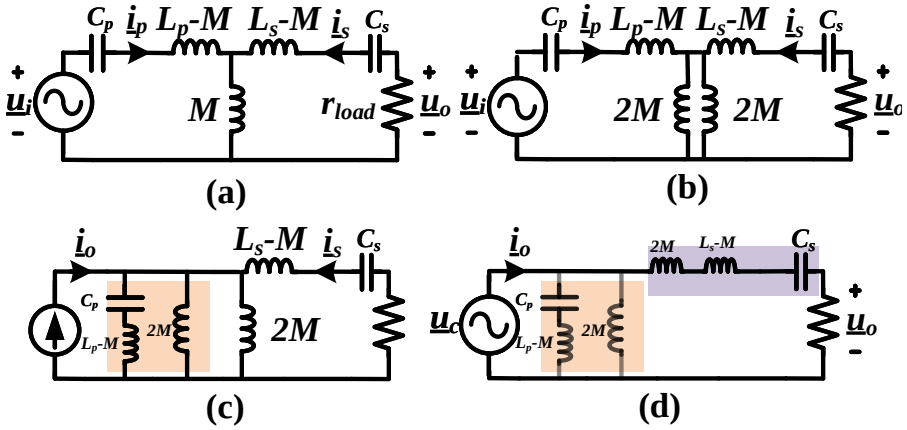

Figure 2.6: SS-Constant Voltage output behaviour at ω_L.

Additionally, we can split the mutual inductance M into two inductances of $2M$ in parallel, as illustrated in Fig. 2.6(b). We feed the input $\underline{u}_i$ with an angular frequency ω_L, where $j\omega_L(L_p - M) + \frac{1}{j\omega_L C_p}$ resonates with $2M$. According to the Thevenin Theorem, the circuit can be equivalently represented as a current source with an internal impedance of $j\omega_L(L_p - M) + \frac{1}{j\omega_L C_p}$, as shown in Fig. 2.6(c). The current source is calculated as $\underline{i}_o = \frac{\underline{u}_i}{j\omega_L(L_p - M) + \frac{1}{j\omega_L C_p}}$, and since $j\omega_L(L_p - M) + \frac{1}{j\omega_L C_p}$ in parallel with $2M$ can be considered an open circuit at resonance, the circuit simplifies further.

Using the Norton Theorem, the current source with internal resistance $2M$ can be transformed into a voltage source $\underline{u}_c = \underline{i}_o \times j\omega_L \cdot 2M$. Since the combination of $2M$ and $L_s - M$ resonates with C_s, this can be approximated as a short circuit, allowing the voltage source $\underline{u}_c$ to be directly applied to the load, thereby exhibiting load-independent voltage source behavior. A more rigorous mathematical proof of this behavior is provided by Zhang W. *et al.* [46]. The operating frequency is calculated by:

$$\omega_L = \frac{\omega_r}{\sqrt{1+k}}, \quad \frac{|\underline{u}_o|}{|\underline{u}_i|} = \sqrt{\frac{L_s}{L_p}} \tag{2.12}$$

Taking a summary, for SS topology, we have a LIC frequency ω_r, and two LIV frequency ω_L and ω_H, additionally, depending on whether the compensation capacitors on the primary and secondary sides are connected in series or parallel, we also have SP (Series-Parallel), PS (Parallel-series), and PP (Parallel-parallel) compensation topologies [47–49] as shown in Fig. 2.7.

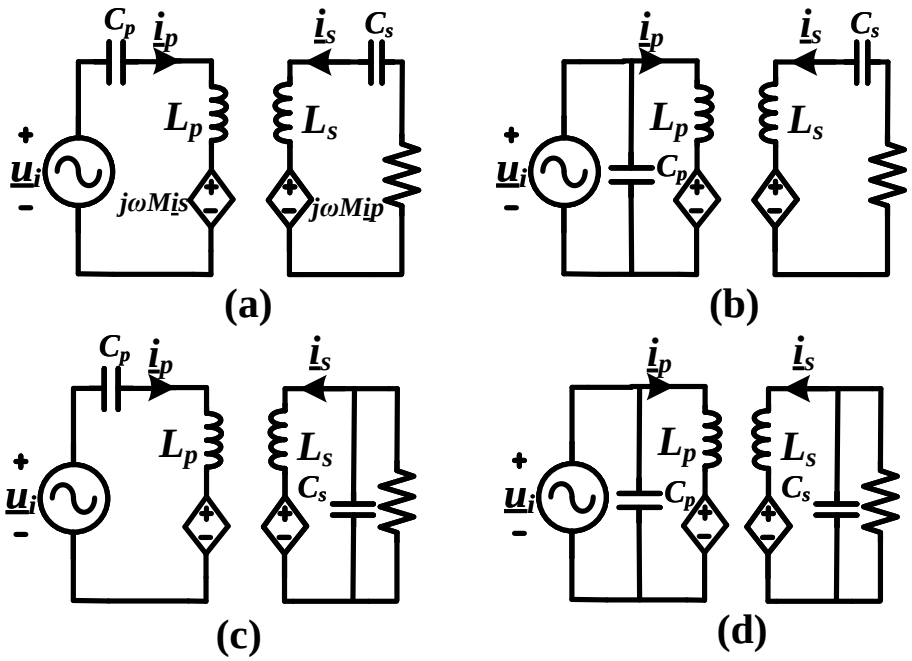

Figure 2.7: (a) SS compensation. (b) PS compensation. (c) SP compensation. (d) PP compensation.

For these four topologies on the secondary side, to maximize output power, we select a capacitor such that $j\omega_r L_s + \frac{1}{j\omega_r C_s} = 0$. However, for the primary compensation capacitor C_p, we aim to achieve a zero phase angle (ZPA) at the input $\underline{u_i}$ to minimize the VA rating. This requirement leads to different capacitor values, as shown in Table 2.1. The table indicates that only the SS capacitor value is independent of the coupling factor M and load resistance R, while the SP topology's capacitor is independent of the load. In contrast, the capacitor values for PS and PP topologies are dependent on both the load and M. In practice, it is desirable for C_p to have a fixed value, unaffected by the coupling factor and load, as this simplifies the design process.

Topology	Primary Capacitance
SS Topology	$C_p = \frac{1}{\omega_r^2 L_p}$
PS Topology	$C_p = \frac{L_p}{\frac{\omega_r^2 M^2}{R} + \omega_r^2 L_p^2}$
SP Topology	$C_p = \frac{1}{\omega_r^2 \left(L_p - \frac{M^2}{L_s}\right)}$
PP Topology	$C_p = \frac{L_p - \frac{M^2}{L_s}}{\left(\frac{M^2 R}{L_s^2}\right)^2 + \omega_r^2 \left(L_p - \frac{M^2}{L_s}\right)^2}$

Table 2.1: Primary Capacitance for Four Basic Compensation Topologies [47].

As illustrated in Fig.2.8, panels (a-c) represent the voltage transfer function, current transfer function, and phase

angle of the input impedance for SS compensation. From these, we observe that ω_r is the Zero Phase Angle (ZPA) frequency for constant current output, while ω_L and ω_H are the constant voltage output frequencies. When operating at frequencies higher than ω_r, the input impedance becomes inductive, meaning the input current lags behind the input voltage. This condition is favorable for achieving Zero Voltage Switching (ZVS), which helps to reduce turn-on losses and mitigate electromagnetic interference (EMI) issues in MHz systems [50]. Conversely, operating at frequencies lower than ω_r can result in Zero Current Switching (ZCS) at turn-off for the inverter.

Typically, in MOSFET inverters, turn-on losses are significantly greater than turn-off losses [51], making ZVS more desirable in wireless power transfer (WPT) applications. Consequently, we can conclude that the SS topology is the most favorable among the four classic topologies, largely due to its primary capacitor being independent of load and coupling conditions.

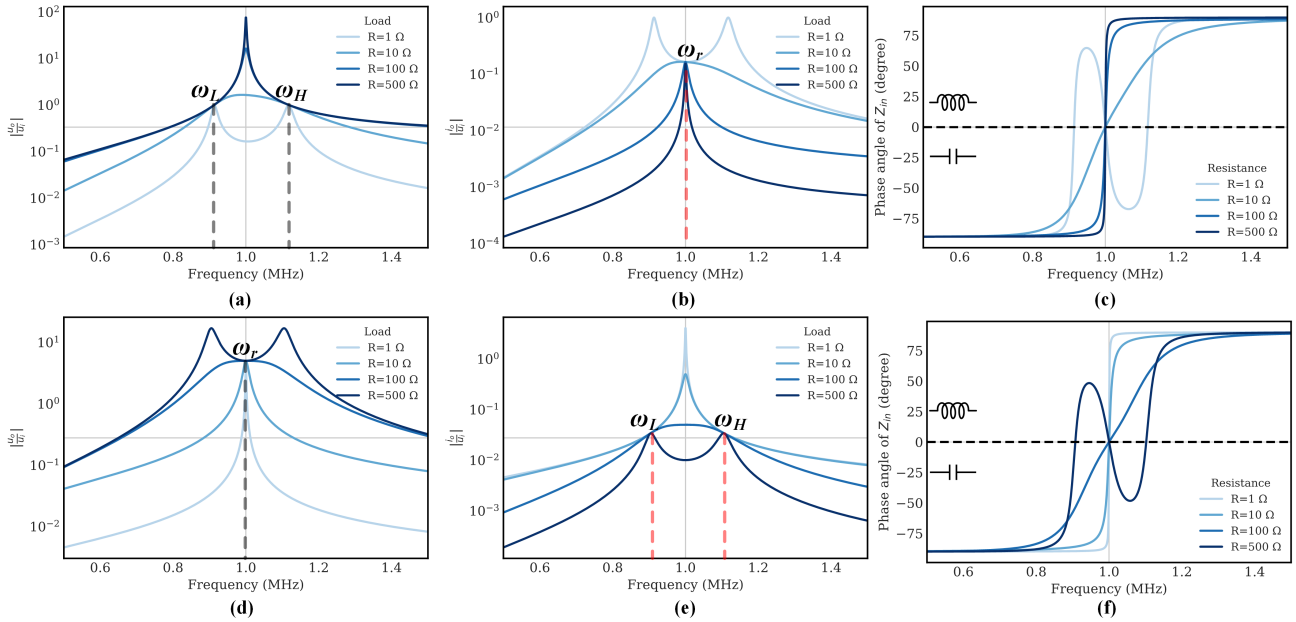

Figure 2.8: (a-c) Voltage transfer function, Current transfer function and phase angle of the input impedance of SS compensation. (d-f) Voltage transfer function, Current transfer function and phase angle of the input impedance of SP compensation.

2.1.3 Maximum Power Efficiency

Take SS as an example, we can not neglect the coil resistance r_p, r_s which cause the losses of the system as shown in Fig. 2.5 (a), the circuit model is given by:

$$(r_p + jX_p)\underline{i}_p + j\omega M\underline{i}_s = \underline{u}_i \tag{2.13}$$

$$j\omega M\underline{i}_p + (r_s + r_{load} + jX_s)\underline{i}_s = 0 \tag{2.14}$$

where $X_p = \omega L_p - \frac{1}{\omega C_p}$, $X_s = \omega L_s - \frac{1}{\omega C_s}$ is the reactance of resonator. Because inductive WPT relies on near-

field coupling, the radiation loss is negligible, and the losses occur due to the parasitic resistances of coil r_p, r_s, the efficiency of the SS system, can be expressed as [52, 53]:

$$\eta = \frac{\text{total output power}}{\text{total input power}} = \frac{|\underline{i}_s|^2 r_{load}}{|\underline{i}_p|^2 r_p + |\underline{i}_s|^2 (r_s + r_{load})} = \frac{r_{load}}{\left(\frac{|\underline{i}_p|}{|\underline{i}_s|}\right)^2 \cdot r_p + r_s + r_{load}}. \tag{2.15}$$

the ratio $\frac{|\underline{i}_p|}{|\underline{i}_s|}$ could be solved by Equ. 2.14

$$\eta = \frac{\omega^2 M^2 r_{load}}{[(r_s + r_{load})^2 + X_s^2] r_p + \omega^2 M^2 (r_s + r_{load})}. \tag{2.16}$$

By solving, the optimal value of X_s for maximizing the efficiency is obtained as

$$\frac{\partial \eta}{\partial X_s} = 0, \quad X_{s\_OPT} = \omega L_s - \frac{1}{\omega C_s} = 0 \tag{2.17}$$

This implies the optimal efficiency is that L_s, C_s forms an LC resonance at this operating frequency. And any deviation of X_s from 0 (like ω_L or ω_H), make X_s looks inductive or capacitive will reduce the efficiency.

Substituting $X_{s\_OPT} = \omega L_s - \frac{1}{\omega C_s} = 0$ into Equ. 3.11 and calculate derivatives respect to r_{load},

$$\frac{\partial \eta}{\partial r_{load}} = 0 \tag{2.18}$$

the optimal values r_{load} can be obtained as,

$$r_{load\_OPT\_\eta} = r_s \sqrt{1 + \frac{\omega^2 M^2}{r_p r_s}} = r_s \sqrt{1 + k^2 Q_p Q_s}, \tag{2.19}$$

where $Q_i = \frac{\omega L_i}{r_i} \quad (i = p \text{ or } s)$ is the quality factor of coil L_i, the maximum efficiency of the system is,

$$\eta_{\text{max}} = \frac{k^2 Q_p Q_s}{\left(1 + \sqrt{1 + k^2 Q_p Q_s}\right)^2}. \tag{2.20}$$

With the below parameter in Tab. 2.2, we could plot the efficiency as a function of the load resistance:

Table 2.2: Simulation Parameters of the SSIPT Converter for Analysis

Parameters	Symbols	Values
Self inductance	L_P, L_S	4.84 μH, 4.84 μH
Coupling coefficient	k	0.174
Equivalent Resistance	R_P, R_S	0.25 Ω, 0.25 Ω
Quality Factor	Q_P, Q_S	202.74
Compensation capacitance	C_P, C_S	5.23 nF, 5.23 nF
Resonant frequency	$\frac{\omega_r}{2\pi}$	1 MHz

As shown in Fig. 2.9, the maximum efficiency η is achieved at 5.29 Ω at the ω_r constant current point. When operating at the ω_L or ω_H constant voltage points, the overall efficiency curve shifts downwards and to the right. At this point, the coil quality factor is 220.74. However, as the load resistance changes to 100 Ω or 0.1 Ω, the efficiency rapidly drops to approximately 40%. This efficiency drop occurs because when r_{load} is large, most of the energy on the secondary side is concentrated in r_{load}, with minimal energy dissipated in r_s. However, for the primary side, the reflected impedance Z_r is inversely proportional to the secondary side impedance. A large r_{load} results in a very small Z_r, causing most of the energy on the primary side to be dissipated in r_p, thereby reducing the overall efficiency. Conversely, when r_{load} is very small, although energy dissipation in r_p on the primary side is minimal, the secondary side r_s dissipates most of the energy. Therefore, only when r_{load} is at a moderate value do both the primary and secondary sides achieve relatively high efficiency, leading to the highest overall system efficiency.

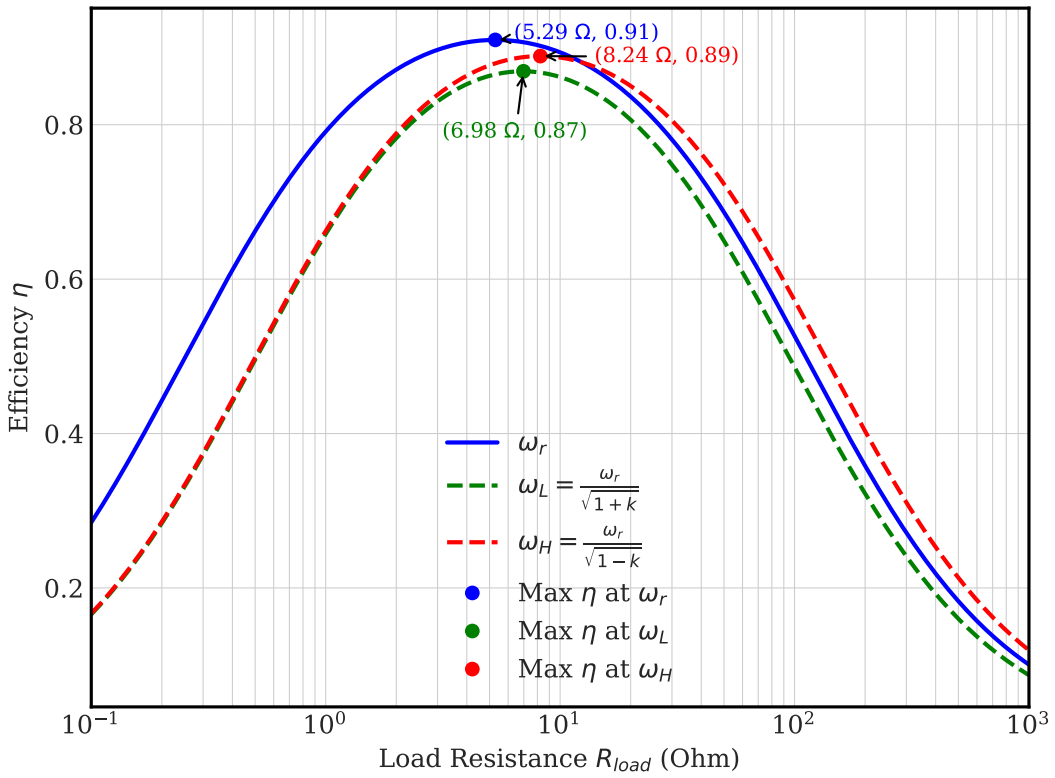

Figure 2.9: Efficiency of an SS WPT system as a function of the load resistance under ω_r Constant Current and ω_L, ω_H Constant Voltage frequency.

It is evident that a higher coil quality factor not only results in a larger amplitude near the resonance frequency and improved selectivity for the resonance frequency, effectively reducing multiple harmonics in the system, but also contributes to enhancing the overall system efficiency. If we reduce the coil resistance by a factor of 10 or 100, the quality factor increases by the same factor, and as illustrated in Fig. 2.10, the efficiency not only increases but

also becomes less sensitive to variations in the load.

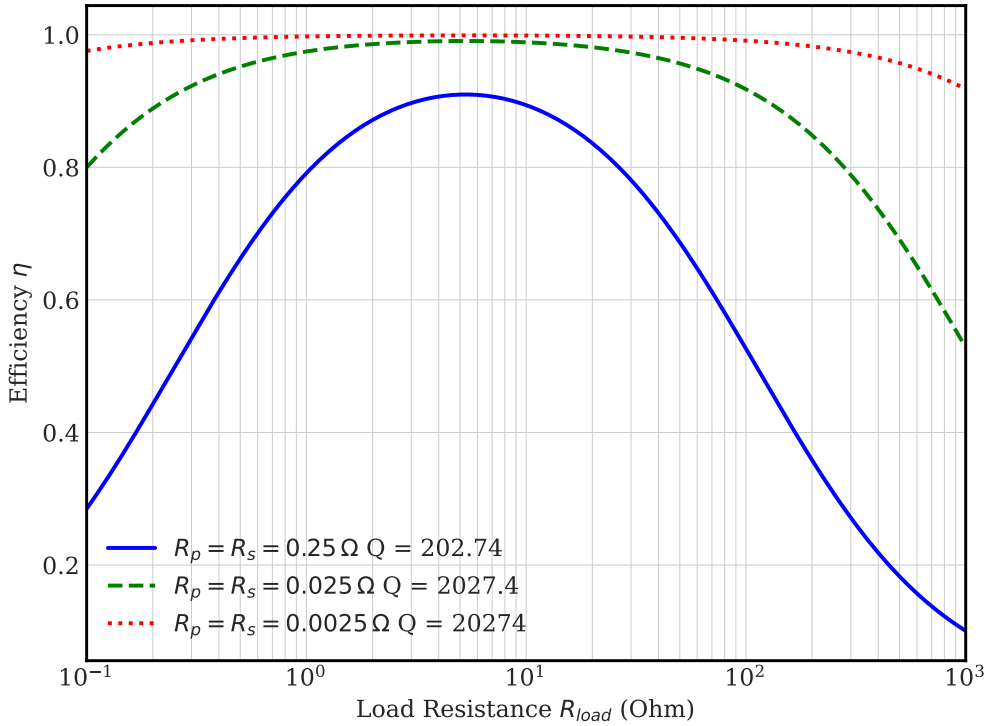

Figure 2.10: Efficiency of an SS WPT system as a function of the load resistance under different quality factor of coils.

2.2 High-voltage WPT Charging Design

Returning to the design objectives of this paper, the goal is to develop a WPT system capable of delivering a high voltage output, specifically to periodically charge a load capacitor from 300V to 330V within 0.5 seconds as shown in Fig. 2.11 (a). We first consider the most straightforward approach: utilizing the SS topology in either CC or CV mode to charge the load through a simple full-wave rectification circuit.

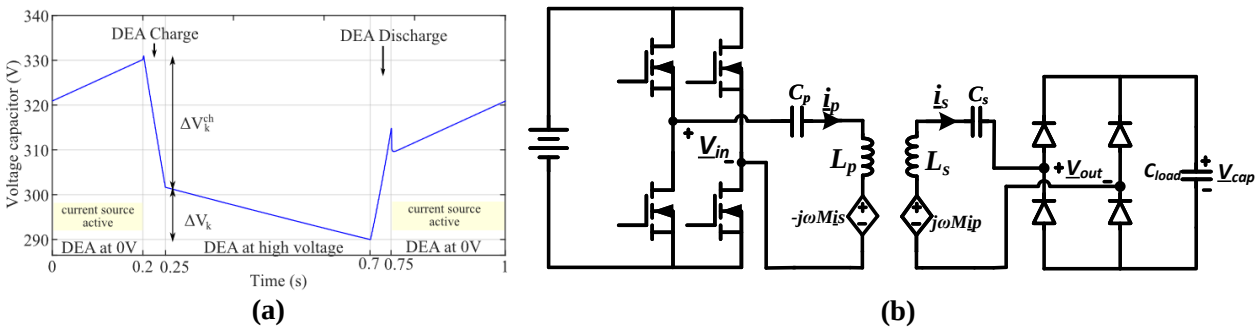

Figure 2.11: (a) Voltage change of load capacitor. Reprinted from [18]. (b) SS topology circuit.

2.2.1 SS-CC Mode

Given an input of 5V and a frequency of ω_r= 1 MHz in the form of a square wave, we can calculate $|\underline{i}_s| = 0.94$ A as a fixed value based on the relationship 2.21. Additionally, the load capacitor is given by $C_{\text{load}} = \frac{Q}{V_{\text{cap}}} = \frac{|\underline{i}_s| \cdot t}{V_{\text{cap}}}$, where Q increases linearly due to the constant current $\underline{i}_s$, resulting in a linear increase in V_{cap}. Consequently, the equivalent resistance of C_{load} also increases linearly according to Ohm's law: $R_{\text{cap}} = \frac{V_{\text{cap}}}{|\underline{i}_s|} = \frac{t}{C_{\text{load}}}$.

$$\underline{i}_s = \frac{\underline{u}_i}{-j\omega_r M}, \tag{2.21}$$

Also it could be concluded that primary current is also increasing linearly from Equ. 2.22

$$\underline{i}_s R_{cap} = j\omega_r M \underline{i}_p \quad \underline{i}_p = \frac{\underline{i}_s t}{C_{load} j\omega_r M} = \frac{\underline{u}_i t}{\omega_r^2 M^2 C_{load}}. \tag{2.22}$$

By setting up the circuit in LTspice simulation software as shown in Tab. 2.3, we can observe the time behavior of V_{in}, I_p, V_{out}, I_s, and V_{cap} in Fig. 2.12.

Table 2.3: Simulation Parameters of the SS-CC Mode for Analysis

Parameters	Symbols	Values
Self inductance	L_P, L_S	4.84 μH, 4.84 μH
Coupling coefficient	k	0.174
Compensation capacitance	C_P, C_S	5.23 nF, 5.23 nF
Input Voltage	V_{in}	5 V
Working frequency	$\frac{\omega_{in}}{2\pi}$	1 MHz
Load capacitance	C_{load}	20 μF
Rectifier Diodes	Vishay VS-E5PX3006	600 V

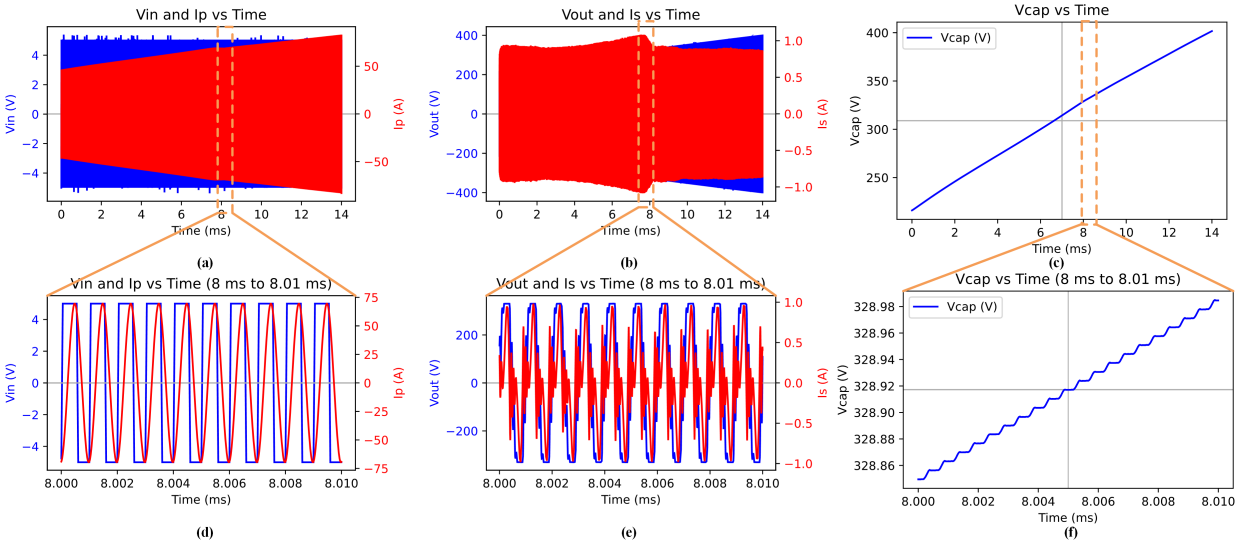

Figure 2.12: (a-f) Time behavior of V_{in}, I_p, V_{out}, I_s, and V_{cap} of SS CC.

From the simulation results, we can see that the secondary current I_s remains almost constant, while V_{out} and V_{cap}

increase linearly. Simultaneously, the primary current I_p also increases linearly. This indicates that as the capacitor voltage increases, the primary current I_p correspondingly rises, reaching nearly 80 A in the simulation. Such a high current is impractical to handle, as it would result in significant currents on the transmitter side, leading to severe heating due to coil resistance in a real scenario.

Additionally, according to Maxwell's equations, the magnetic field generated by the primary current would be extremely large, potentially exceeding the ICNIRP [54, 55] limits for medical devices.

$$H(t,x) = I(t) \cdot \frac{1}{2} \cdot \frac{r^2}{(x^2+r^2)^{3/2}} = 697.2 \quad \text{(A/m)} \tag{2.23}$$

where: I(t) - current (A) at time t (s), r - radius of the loop (m), here we suppose 42.5 mm, x - location (m) from the center of the loop (the center is located at point x = 0); here we suppose 20 mm,

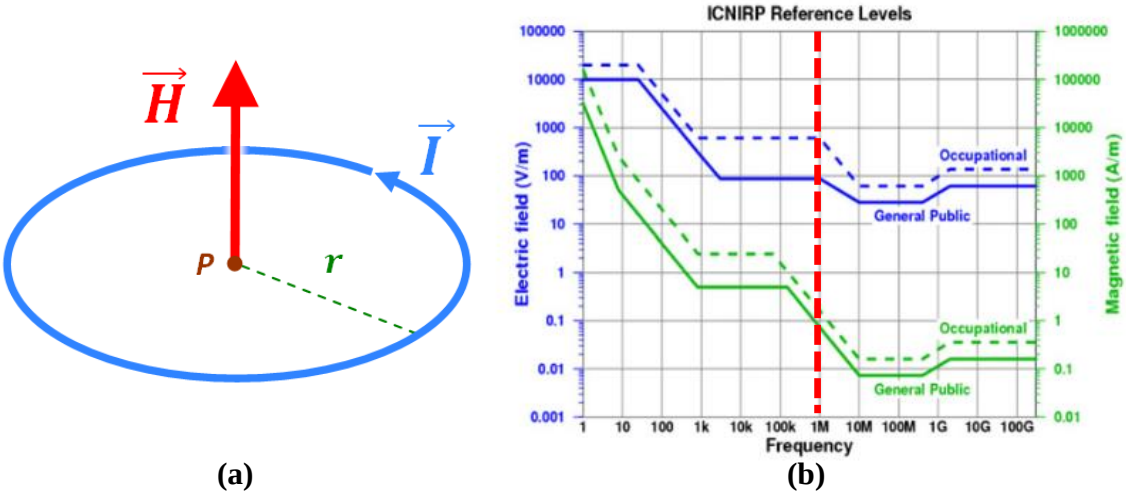

(a) (b)

Figure 2.13: (a) Schematic of H along axis of circular current loop [56]. (b) ICNIRP [55].

Except above, it can be observed that the charging speed in CC mode is very fast, taking only 2 ms to charge a 20 μF capacitor from 300 V to 330 V. However, unlike CV mode, which automatically stops charging upon reaching the threshold, CC mode does not have this feature. Therefore, we need to design an additional voltage detection circuit on the receiver side to control the start and stop of charging, which will increase the size of the implanted device.

2.2.2 SS-CV Mode

Compared to the risk of overcharging in CC mode [41], the drawback of CV charging is that when the capacitor voltage is low, the charging current can be quite large, and it exhibits an exponential decay in Equ. 2.24 (where $\tau = RC$). However, in the context of periodically charging the capacitor from 300 V to 330 V—similar to the final stage of battery charging—CV mode is more suitable.

$$V(t) = V_0 + (V_{\text{initial}} - V_0) \cdot e^{-\frac{t}{\tau}}, \quad I(t) = \frac{V_0 - V_{\text{initial}}}{R} \cdot e^{-\frac{t}{\tau}} \tag{2.24}$$

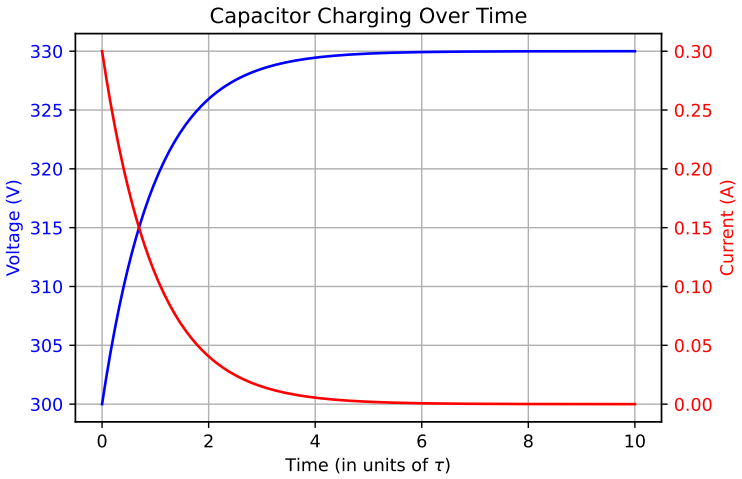

Figure 2.14: Capacitor Charging Voltage and Current Over Time.

In SS-CV mode, it is preferable to operate at ω_H due to its ZVS properties. At this frequency, the voltage gain $G_v = \frac{V_{out}}{V_{in}}$ can be calculated using Equ. 2.26 [46,53,57]. Thus, rather than resorting to complex and space-consuming solutions such as using a single transmitting coil with multiple receiving coils in series [58], or multiple transmitting coils in series with multiple receiving coils in series (ISOS) [59], the simplest way to achieve a high output voltage is to increase L_s relative to L_p, as indicated by Equ. 2.26.

$$\omega_r = \frac{1}{\sqrt{L_p C_p}} = \frac{1}{\sqrt{L_s C_s}}, \quad \omega_L = \frac{\omega_r}{\sqrt{1+k}} \quad \omega_H = \frac{\omega_r}{\sqrt{1-k}}, \tag{2.25}$$

$$G_v(\omega_H) = \frac{|V_{out}|}{|V_{in}|} = \sqrt{\frac{L_s}{L_p}}. \tag{2.26}$$

Given an input of 15V and a frequency of $\omega_r = 1$ MHz in the form of a square wave, assume $L_p = 1\ \mu$H. (L_p should not be too small, as a small inductance implies lower magnetic flux density, which can lead to reduced coupling efficiency between the transmitting and receiving coils. This directly impacts both the transmission distance and efficiency. Moreover, it makes the system more susceptible to interference or parasitic effects.) To achieve $V_{\text{out}} = 330$ V, we require $L_s = 484\ \mu$H. Here, we assume that the coil is a flat coaxial half-filled disc coil as shown in Fig.2.15. Due to the volume constraints of the implanted coil, the coil diameter is limited to 85 mm, and the distance between the two coils is assumed to be 20 mm. Based on Leibl *et al.*'s finite element simulation, the required number of turns can be calculated using Equ. 2.27 [60]:

$$L \approx 0.76 \mu_0 d N^2. \tag{2.27}$$

For the primary coil, N_p is approximately 3 turns, and for the secondary coil, N_s is approximately 78 turns. At this point, we can no longer neglect the coil resistance, which can be considered as consisting of both DC and AC components [61]:

$$R_{\text{total}} = R_{DC} + R_{AC}, \quad R_{DC} = \frac{\rho \times l}{A_{\text{total}}}, \quad R_{AC} \approx R_{DC} \times \left(1 + k \times \sqrt{f}\right). \tag{2.28}$$

where: - ρ is the resistivity of the wire (for copper, approximately $1.68 \times 10^{-8}\,\Omega \cdot$ m). - l is the total length of the coil. - A_{total} is the total cross-sectional area of the Litz wire. - f is the operating frequency (in Hz). - k is an empirical constant that depends on the number of strands, strand diameter, and the braiding pattern of the Litz wire.

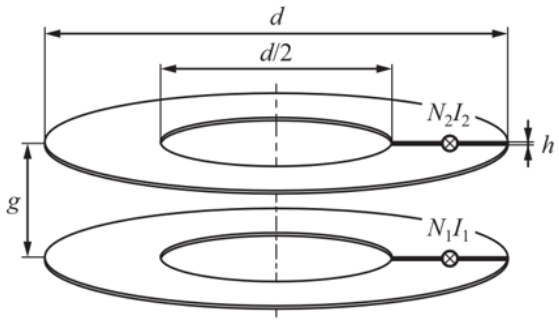

Figure 2.15: Pair of magnetically coupled flat coaxial half-filled disc coils with dimensions. The total ampere-turns NI of each coil are assumed to be homogeneously distributed over the coil cross-section. Reprinted from [60].

Such a high number of turns within a limited space poses significant challenges for the manufacturing process. To achieve 78 turns, the coil cross-sectional area must be reduced, which in turn increases the DC and AC internal resistance as described by Equ. 2.28. Simulating this setup in LTspice as shown in Tab. 2.4, with L_s set to 484 μH and adding 10 Ω of internal resistance to the secondary side, we can observe from the results in Fig. 2.16 that the primary current remains very high, exceeding the safety limit. Moreover, with L_p being much smaller than L_s, achieving good coupling between L_s and L_p becomes challenging, making it difficult to effectively transfer power from L_s. Additionally, increasing L_s inevitably raises the internal resistance of the coil, leading to higher power losses in the implanted device. These losses, which manifest as heat, are difficult to dissipate from within the body, potentially posing a safety risk to the patient.

Table 2.4: Simulation Parameters of the SS-CV Mode for Analysis

Parameters	**Symbols**	**Values**
Self inductance	L_P, L_S	1 μH, 484 μH
Coupling coefficient	k	0.174
Compensation capacitance	C_P, C_S	25.33 nF, 52.33 pF
Equivalent Resistance	R_S	10 Ω
Input Voltage	V_{in}	15 V
Working frequency	$\frac{\omega_{in}}{2\pi}$	1.1 MHz
Load capacitance	C_{load}	20 μF
Rectifier Diodes	Vishay VS-E5PX3006	600 V

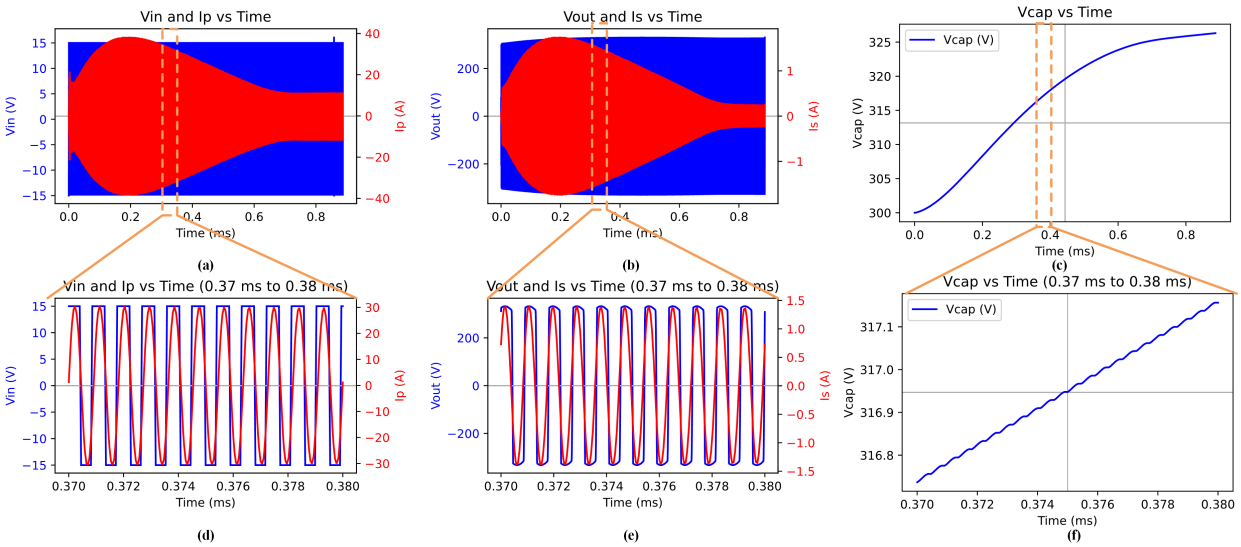

Figure 2.16: (a-f) Time behavior of V_{in}, I_p, V_{out}, I_s, and V_{cap} in the SS CV configuration.

Based on the discussion above, the WPT system combined with a simple four-diode full-wave rectifier is insufficient to meet our design goals. To overcome the issues of excessive primary current stress in CC mode and the need for a large inductance in the receiving coil for CV mode, we need to consider using a new rectification circuit—the Cockcroft-Walton Voltage Multiplier. This circuit can convert a low-voltage AC input into a high-voltage DC output. The principles and characteristics of this circuit will be introduced in the next chapter.

Chapter 3

Cockcroft-Walton Voltage Multiplier

3.1 Principle of Cockcroft-Walton Voltage Multiplier (CW-VM)

The Cockcroft-Walton multiplier (also called Greinacher multiplier [62]), named after the physicists John Douglas Cockcroft and Ernest Thomas Sinton Walton, is a high-voltage generating electrical circuit [63]. It was invented in the early 20th century and is particularly noted for its role in the first artificial nuclear disintegration in 1932 [64]. This multiplier uses a cascaded array of capacitor-diode pairs to convert a low AC input into a high DC voltage as shown in Fig. 3.1. Its design eliminates the need for a high-voltage transformer, making it a cost-effective solution for many high-voltage applications including X-ray imaging [65], electrostatic precipitator [66], photomultiplier [67], RF energy harvesting of IoT [68], micro aerial vehicles (MAVs) [69, 70], etc.

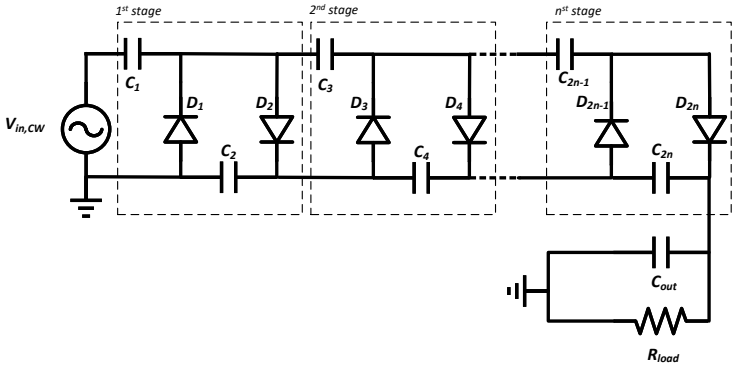

Figure 3.1: Schematic of a Cockcroft-Walton VM.

3.1.1 CW-VM Without Load

As shown in Fig. 3.2, when a sinusoidal wave with an amplitude V_{in} is applied to the input of a CW-VM, during the negative half-cycle, the power source charges the capacitors C_1, C_3, C_{2n-1} through the diodes D_1, D_3, D_{2n-1}. During

the positive half-cycle, the power source charges the capacitors C_2, C_4, C_{2n} through the diodes D_2, D_4, D_{2n}. In the absence of a load, the voltage across each capacitor will reach a saturation value: C_1 will be charged to V_{in}, while all other capacitors will be charged to $2V_{\text{in}}$. As a result, we obtain an output voltage of $2nV_{\text{in}}$ at the right end of C_{2n}.

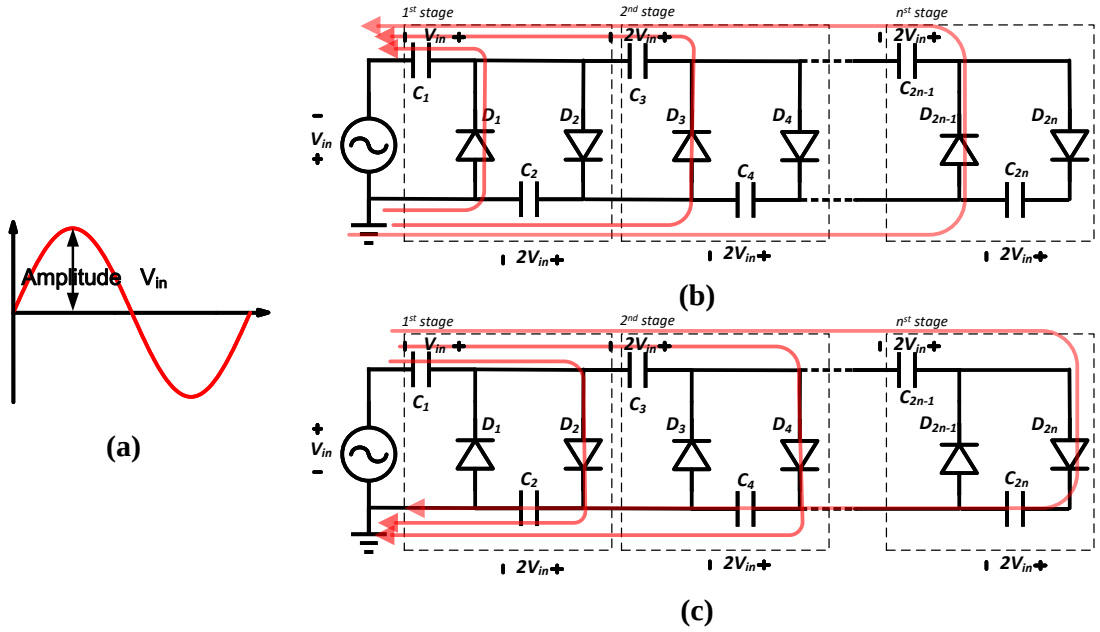

Figure 3.2: Schematic of a Cockcroft-Walton VM without Load.

3.1.2 CW-VM in Steady State

When the output load capacitor C_{out} of the CW-VM reaches a stable voltage, only the load resistor continues to consume current. At this point, the circuit operates in a steady state with a consistent output voltage pattern. Here, we assume that C_1' and C_2' are large enough to maintain a relatively constant output voltage across the load, so that the output current i_R remains continuous with only a small ripple. The amount of charge delivered to the load during one switching cycle $1/f$ is denoted by q.

The column of capacitors C_1, C_2 is known as the oscillating column (also known as the coupling column), while the column of C_1', C_2' is called the smoothing column.

The push phase [Fig. 3.3 (b)] is the interval between $t = 0$ and $t = t_1$. At t_1, the voltage source reaches its peak in the positive cycle. We assume that the charging of the capacitors happens instantaneously, where C_1 and C_2 charge C_1' and C_2' to restore the voltage drop on C_1' and C_2'.

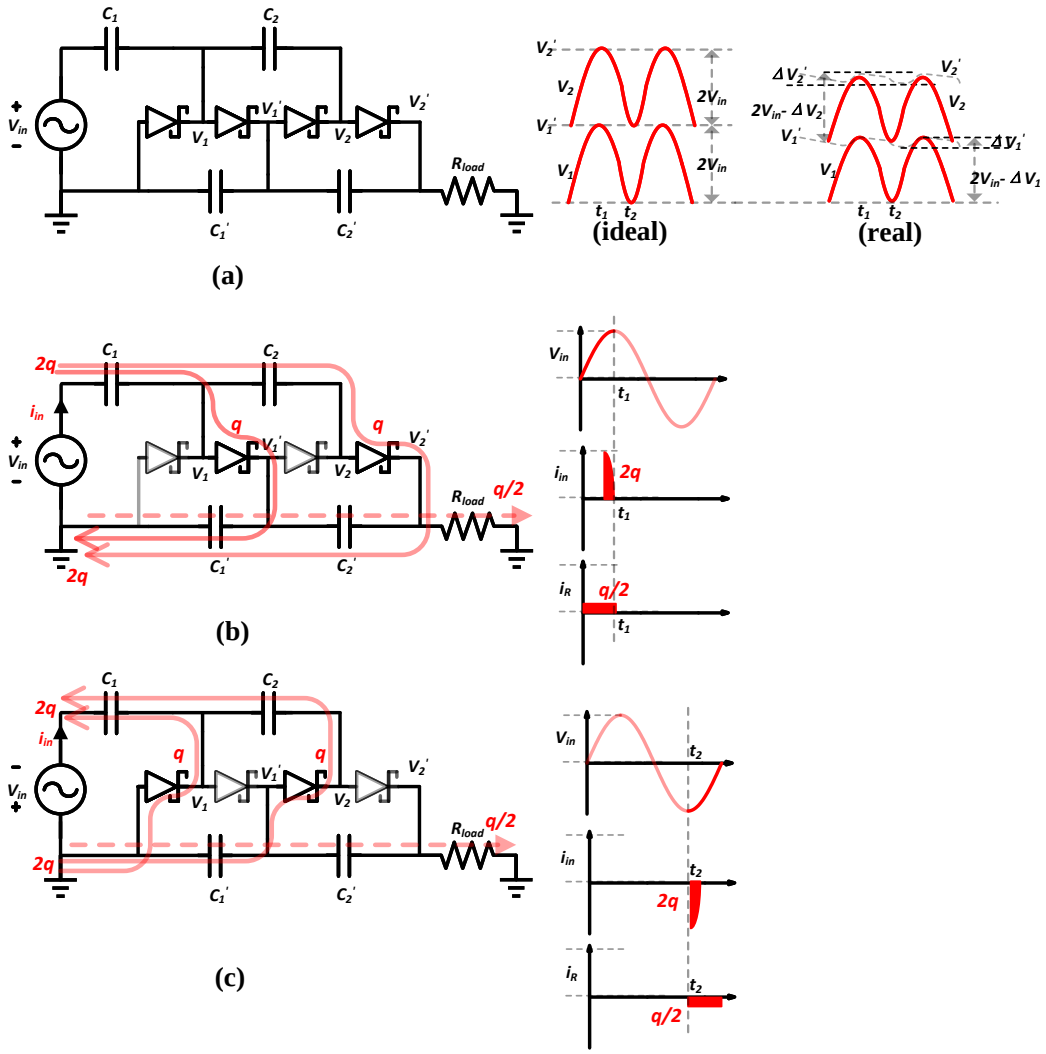

Figure 3.3: (a) Schematic. (b) Charge flow during the push phase. (c) Charge flow during the pull phase.

The pull phase [Fig. 3.3 (c)] is the interval between $t = t_1$ and $t = t_2$. At t_2, the voltage source reaches its peak in the negative cycle, where C_1' and C_2' charge C_1 and C_2 to restore the voltage drop on C_1 and C_2 caused by the previous charging of C_1' and C_2'.

Therefore, it can be observed that the voltages across C_1, C_2, C_1', and C_2' cannot remain stable because the capacitance values cannot be ideally infinite. The current flowing through the coupling column C_1, C_2 will cause a voltage drop ΔV on V_1 and V_2, and the current flowing through the smoothing column C_1', C_2' will cause a peak-to-peak voltage ripple $\Delta V'$ on V_1' and V_2'.

we could calculate the peak value of the output voltage V_2', denoted by $V_{2,max}'$, can be expressed as:

$$v'_{2,\text{max}} = 4V_{in} - \Delta V \tag{3.1}$$

where

$$\Delta V = \Delta V_1 + \Delta V_1' + \Delta V_2 \tag{3.2}$$

$$= \sum_{k=1}^{2} (\Delta V_k + \Delta V_k') - \Delta V_2'. \tag{3.3}$$

The output peak-to-peak ripple which we denote by δV is, by definition:

$$\delta V = \Delta V_2'. \tag{3.4}$$

The average output voltage V_{out} is

$$V_{\text{out}} = v_{2,\text{avg}}' \approx 4V_{in} - \Delta V - \frac{1}{2}\delta V. \tag{3.5}$$

Additionally, there is a similar structure called the Dickson VM. The key difference between the Dickson VM and the CW VM is that in the Dickson VM, all the capacitors are connected in parallel and are subject to the same voltage, which results in higher voltage stress on the capacitors. Furthermore, the current flowing through each capacitor is q, which means that the voltage drop and ripple in the Dickson VM are much smaller than in the CW VM, especially at higher stages. In contrast, the capacitors in the CW VM are connected in series, leading to lower voltage stress on each capacitor. Moreover, a trade-off between the two can be achieved, as shown in Fig. 3.4 (c), to balance voltage stress and ripple drop, as illustrated in Table 3.1.

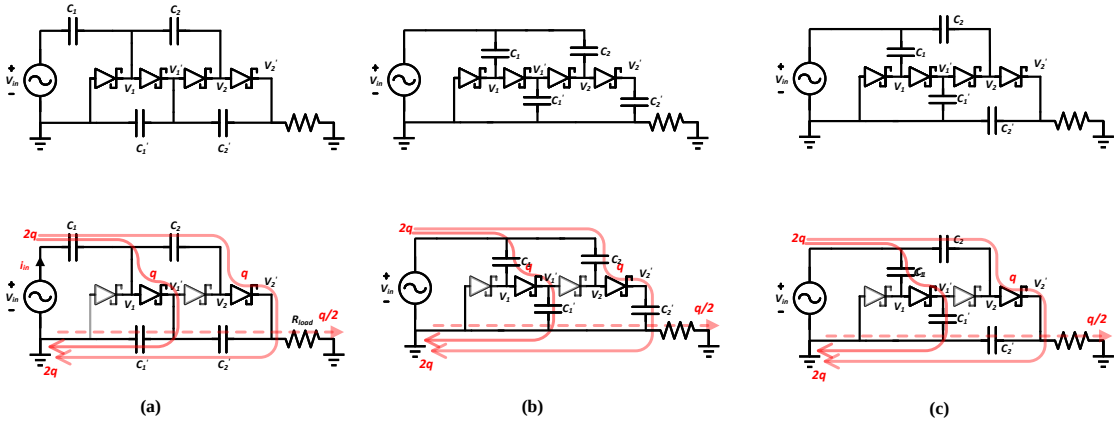

Figure 3.4: Two-stage voltage multipliers in three different topologies. (a) Cockcroft–Walton. (b) Dickson. (c) (1x2) Hybrid.

The above content is based on these references. Due to space limitations, for a more detailed explanation, please refer to [71–73].

For an $m \times n$ cascode hybrid structure, we can derive the corresponding formulas.

Table 3.1: Voltage Drops at Each Node in Two-Stage Multipliers of Fig. 3.4

k	Cockcroft-Walton		Dickson		Hybrid	
	ΔV_k	$\Delta V_k'$	ΔV_k	$\Delta V_k'$	ΔV_k	$\Delta V_k'$
1	$\frac{2q}{C_1}$	$\frac{2q}{C_1'}$	$\frac{q}{C_1}$	$\frac{q}{C_1'}$	$\frac{q}{C_1}$	$\frac{q}{C_1'}$
2	$\frac{2q}{C_1}+\frac{q}{C_2}$	$\frac{2q}{C_1'}+\frac{q}{C_2'}$	$\frac{q}{C_2}$	$\frac{q}{C_2'}$	$\frac{q}{C_2}+\frac{2q}{C_2}$	$\frac{2q}{C_2'}$

$$\Delta V = \frac{q}{C}\left[m^3\left(\frac{2}{3}n^2\right)+m^2\left(-n^2+\frac{3}{2}n\right)+m\left(\frac{1}{3}n^2+\frac{1}{2}n-1\right)\right] \tag{3.6}$$

$$\delta V = \frac{q}{C}\left[m^2\left(\frac{n}{2}\right)+m\left(1-\frac{n}{2}\right)\right] \tag{3.7}$$

$$V_{\text{out}} = v'_{mn,\text{avg}} \approx 2mnV_{in} - \Delta V - \frac{1}{2}\delta V \tag{3.8}$$

For CW VM, it means n=1, we get:

$$\Delta V = \frac{q}{C}\left[\frac{2}{3}m^3+\frac{1}{2}m^2-\frac{1}{6}m\right] = \frac{I_{out}}{fC}\left[\frac{2}{3}m^3+\frac{1}{2}m^2-\frac{1}{6}m\right] \tag{3.9}$$

$$\delta V = \frac{q}{C}\left[\frac{1}{2}m^2+\frac{1}{2}m\right] = \frac{I_{out}}{fC}\left[\frac{1}{2}m^2+\frac{1}{2}m\right] \tag{3.10}$$

Additionally, in a CW VM, the lower-stage capacitors experience higher current, leading to larger voltage drops and ripples. To mitigate these effects, we can also use larger capacitance values for the lower-stage capacitors [74]. However, for simplicity, it is common practice to use capacitors of the same value throughout the circuit.

However, in reality, it cannot be assumed that charging is instantaneous. Instead, the diodes conduct sequentially from the highest to the lowest stage [75–77]. For example, in a third-level CW VM:

1. **Mode 1 Fig. 3.5 (a)**: All diodes are blocked, and no current flows. Capacitors C_2, C_4, and C_6 charge the load, while C_1, C_3, and C_5 are floating.

2. **Mode 2 Fig. 3.5 (b)**: The positive half-cycle begins. Diodes D_2 and D_4 are still blocked, while D_6 conducts first. Odd capacitors (C_1, C_3, C_5) are discharged, and even capacitors (C_2, C_4, C_6) are charged, while the capacitors also supply current to the load.

3. **Mode 3 Fig. 3.5 (c)**: As v_{d4} equals v_{d3}, diode D_6 is blocked, and D_4 conducts. Capacitors C_2 and C_4 are charged, while C_1 and C_3 are discharged, continuing to supply load current.

4. **Mode 4 Fig. 3.5 (d)**: D_4 is blocked, and D_2 begins to conduct. Capacitor C_2 is charged while C_1 is discharged. Capacitors continue to supply load current.

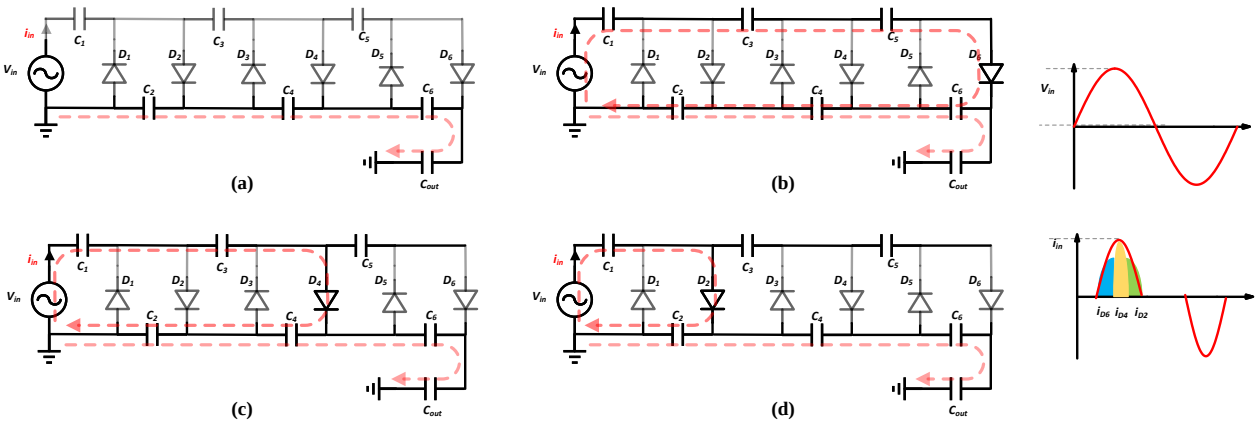

Figure 3.5: Circuit Modes of CW with Capacitive Load.

3.2 Design of Cockcroft-Walton Voltage Multiplier

In this case, the input voltage V_{in} for the CW is 15V, and we require an output of at least 330V. To allow some margin, we can target an output of 360V, which means a 12-stage CW multiplier is needed. We select an input frequency of 1 MHz. We can calculate the relationship between V_{out} and the capacitance C from Equ. 3.9, 3.10, as shown in the Fig. 3.6. To minimize the volume, we choose MLCC capacitors with a 0603 package. After filtering all options on Mouser, we selected the GRM188R72A104KA35D capacitor with a rating of 100 VDC, 100 nF, X7R dielectric, as a trade-off between volume, capacitance, voltage rating, and capacitance stability under applied voltage.

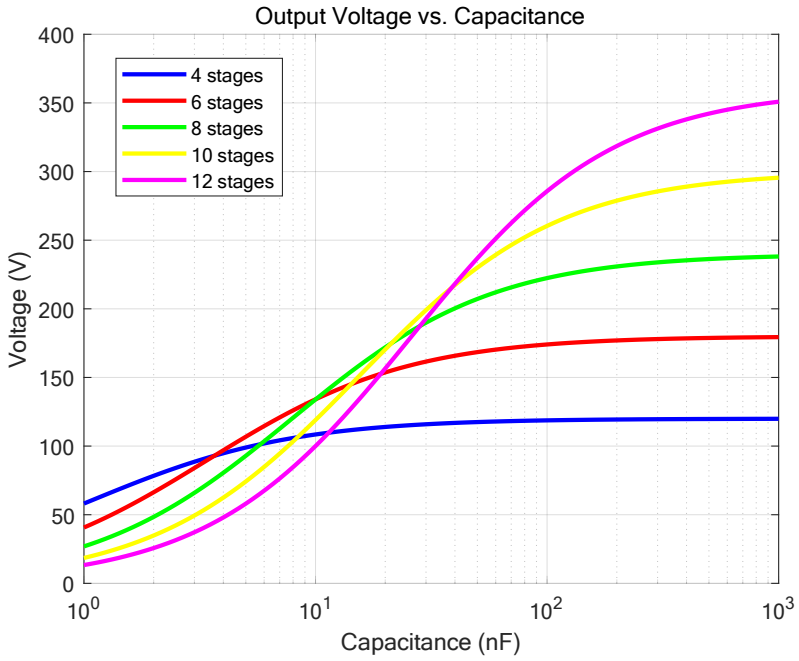

Figure 3.6: Influence of the number of stages and capacitance on the output voltage of CW with 47k Ω load.

According to the formulas below, to reduce the voltage drop (lower the equivalent internal resistance and improve charging speed), we can design the circuit as a 6x2 hybrid CW-Dickson structure.

$$V_{\text{out}} = v'_{mn,\text{avg}} \approx 2mnV_{in} - \Delta V - \frac{1}{2}\delta V \tag{3.11}$$

$$\Delta V = \frac{q}{C}\left[m^3\left(\frac{2}{3}n^2\right) + m^2\left(-n^2 + \frac{3}{2}n\right) + m\left(\frac{1}{3}n^2 + \frac{1}{2}n - 1\right)\right] \tag{3.12}$$

$$= \frac{I_{out}}{fC}\left[m^3\left(\frac{2}{3}n^2\right) + m^2\left(-n^2 + \frac{3}{2}n\right) + m\left(\frac{1}{3}n^2 + \frac{1}{2}n - 1\right)\right] \tag{3.13}$$

$$\delta V = \frac{q}{C}\left[m^2\left(\frac{n}{2}\right) + m\left(1 - \frac{n}{2}\right)\right] = \frac{I_{out}}{fC}\left[m^2\left(\frac{n}{2}\right) + m\left(1 - \frac{n}{2}\right)\right] \tag{3.14}$$

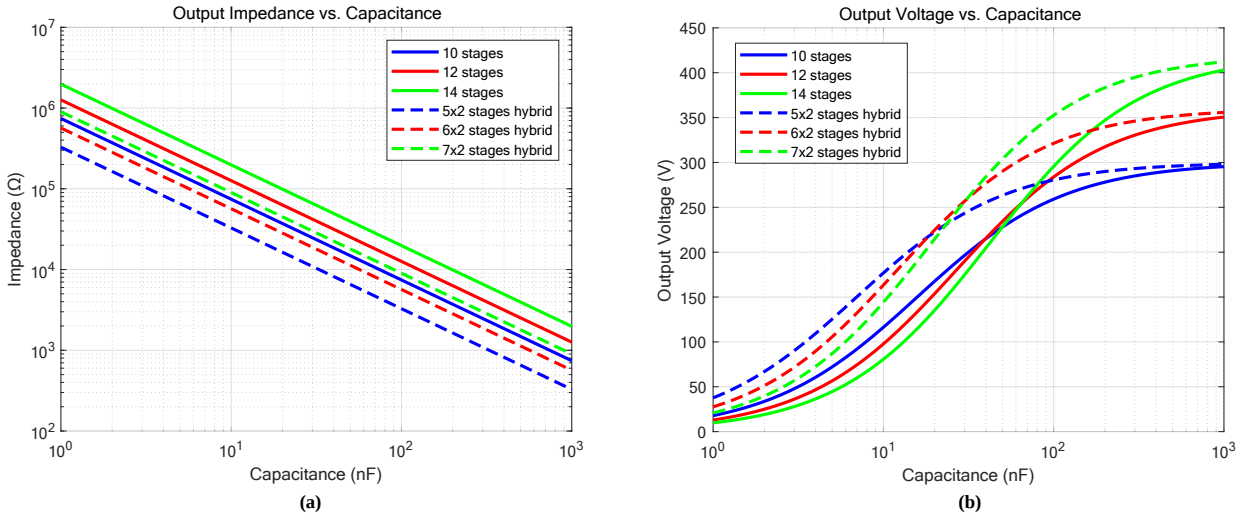

Figure 3.7: Comparison of output impedance and output voltage of CW or Hybrid CW-Dickson with 47k Ω load.

As shown in the Fig. 3.7, by using the 6x2 Hybrid structure, the output internal resistance is effectively reduced, and the output voltage is increased. However, the voltage stress on the capacitors is doubled, which can lead to a decrease in capacitance. Although this effect is not accounted for in the Fig. 3.7, even with the reduction in capacitance, the output voltage can still be improved.

For the diodes, since we are dealing with high-frequency currents, we need to use Schottky diodes. Due to their unique construction (metal-semiconductor junction), Schottky diodes have negligible recovery time. However, they typically have lower voltage ratings. Here, we have selected the SS16HE from onsemi, which has a slightly larger footprint than the 0603 capacitors. It has a voltage rating of 60 V, can handle a continuous current of 1 A and a peak surge current of 25 A, with a forward voltage drop of only 0.51 V at 0.5 A. The recovery time is 8.3 ns, which is minimal

compared to the 1000 ns period at 1 MHz.

The final design of the Hybrid CW circuit is shown in Fig. 3.8. In this design, a MOSFET switch is added to the CW circuit, controlled by an ATTINY406-SNR MCU, allowing us to control the activation or interruption of the CW circuit on the receiver side without needing to stop the operation of the transmitting coil. This means that even when the CW circuit is turned off, the transmitting coil can continue to operate and supply energy to other loads. Additionally, a load circuit is included, where capacitors or resistors can be soldered. The assembled PCB is shown in Fig. 3.9. To prevent the reverse flow of charge from the load capacitor, a high-voltage diode, SBR1U400P17 (1A, 400V), is added to the output side of the CW circuit.

The MCU circuit can control the MOSFET by decoding the signal from the transmitter side using ASK (Amplitude Shift Keying), please refer [18].

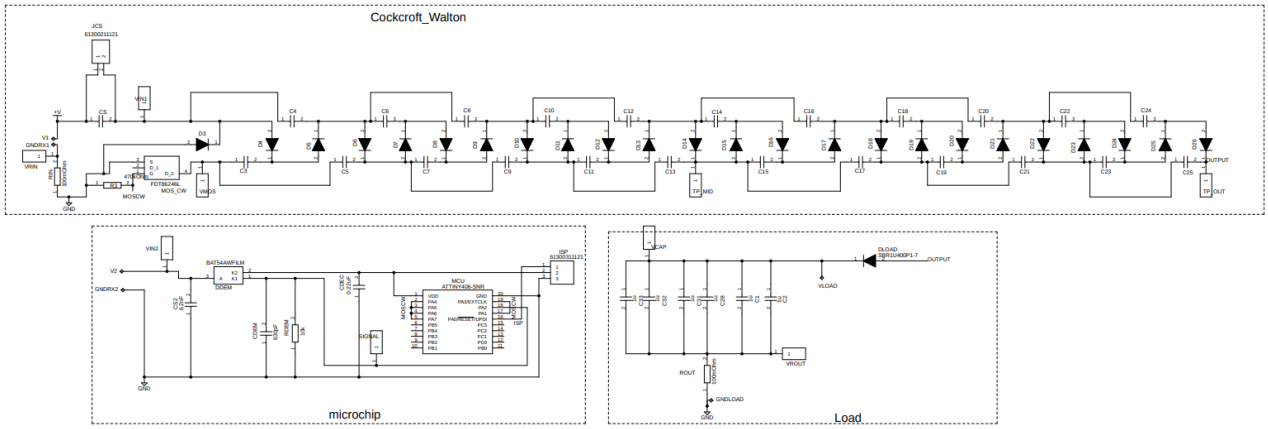

Figure 3.8: Final Hybrid CW Circuit diagram.

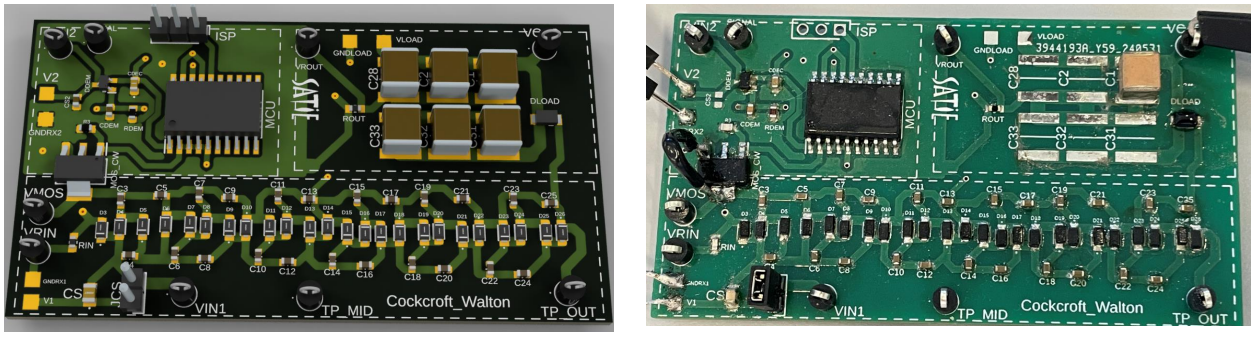

Figure 3.9: PCB of Hybrid CW VM.

Under an input of $V_{\text{in}} = 2$ V at 100 kHz, the rise time under no-load conditions is approximately 20 ms. The experimental results and simulation results show very good agreement as shown in Fig. 3.10.

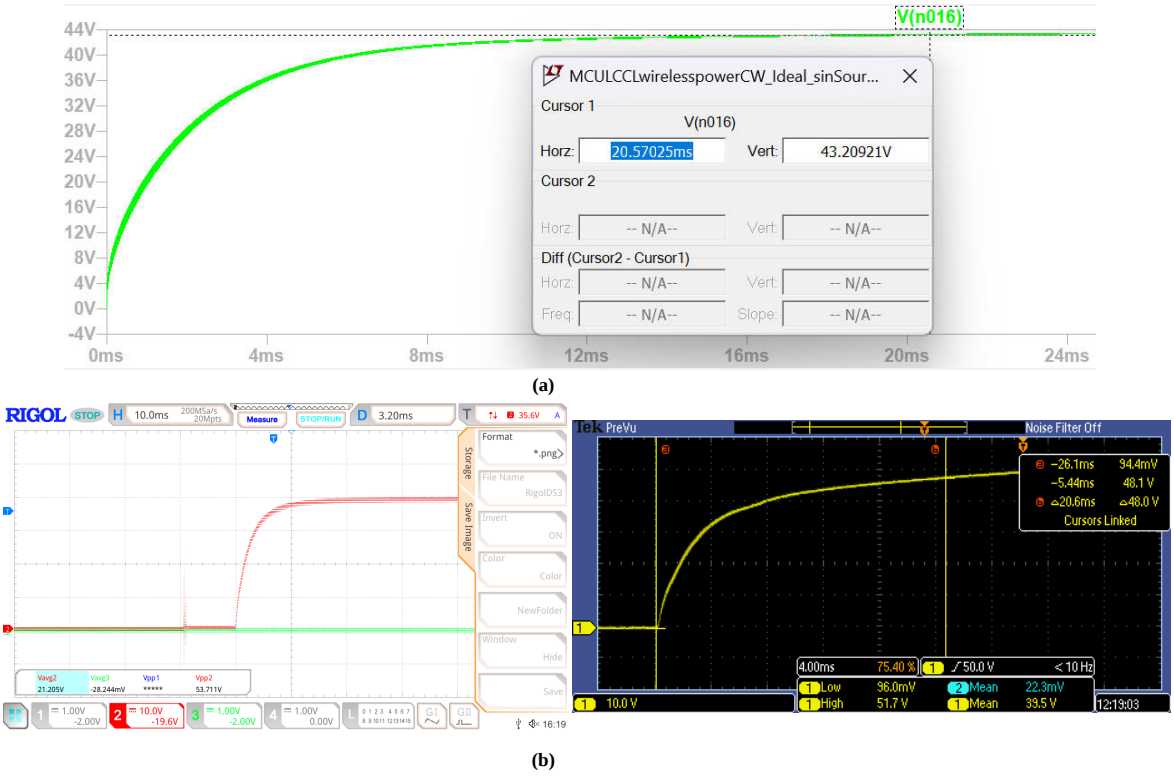

Figure 3.10: Rise time of Hybrid CW VM without Load.

3.2.1 Efficiency of Hybrid CW VM

To estimate the efficiency of the circuit with a 47k ohm load resistor, we can calculate the losses caused by the capacitor's Equivalent Series Resistance (ESR) and the forward voltage drop of the Schottky diodes. The relevant power loss equations are:

- **Capacitor ESR Loss**:

$$P_C = \text{ESR} \cdot I_{C,\text{rms}}^2$$

- **Schottky Diode Conduction Loss**:

$$P_{\text{con}} = U_{D0} \cdot I_{F,\text{av}}$$

The calculated power loss due to the capacitor's ESR is approximately 0.0277355 W, and the power loss in the diode is approximately 0.1088085 W. The input power is calculated to be 2.1335 W as shown in Fig. 3.11.

Based on LTspice simulation results, the capacitor's ESR loss is approximately 0.0302932 W, the diode loss is about 0.10819 W, and the input power is approximately 2.1638 W as shown in Fig. 3.11.

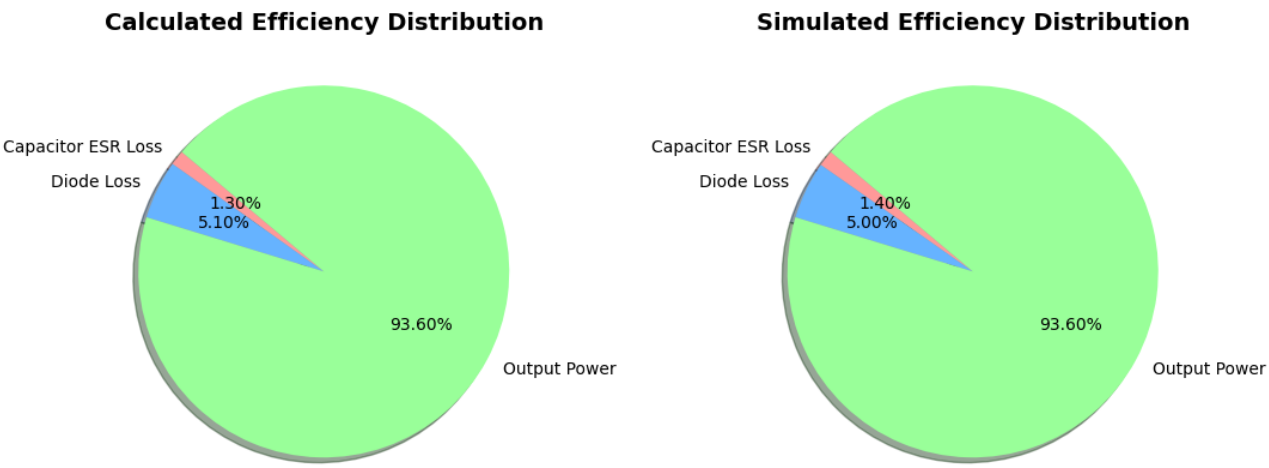

Figure 3.11: Efficiency Distribution of Hybrid CW VM.

Chapter 4

LCC-S Based WPT Powering VM for High Voltage Capacitor Charging

4.1 LCC-S Compensation Topology

Although the SS compensation topology has the advantages of a simple structure, a primary compensation capacitor that is independent of load and coupling coefficient variations, and the ability to operate at load-independent voltage (LIV) and load-independent current (LIC) points, it also has several drawbacks:

1. If operating at the CC (LIC) frequency ω_r, under low coupling or misalignment conditions, the controlled voltage source induced by the coupling, $j\omega_r M\underline{i}_s$, will almost disappear. This results in the primary side resonating only with its capacitance C_p and inductance L_p, effectively creating a short circuit that may generate excessively high currents, potentially damaging the circuit.

2. If operating at the $\omega_H = \frac{\omega_r}{\sqrt{1-k}}$ CV (LIV) frequency, any change in the coupling condition between the two coils, such as the air gap varying in real-time in a transcutaneous energy transmission system when the patient is breathing [49, 78, 79], will cause this CV frequency to shift. Operating at a fixed frequency under these conditions will result in the output voltage no longer being independent of the load as shown in Fig. 4.1.

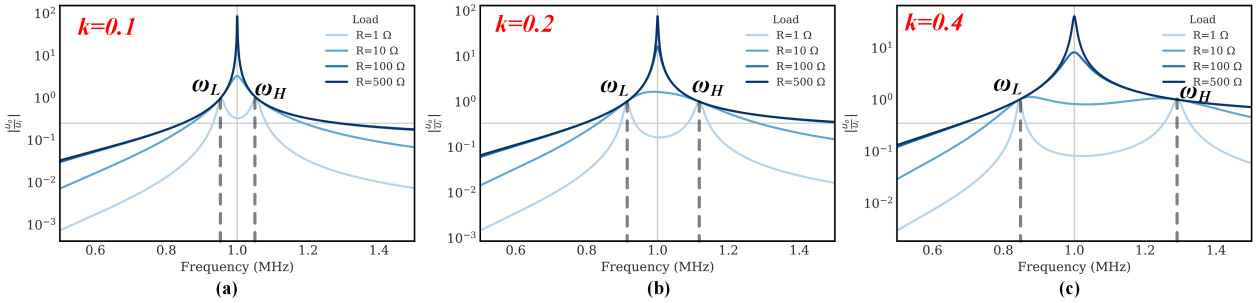

Figure 4.1: SS-Constant Voltage output behaviour at different k.

To address these issues, researchers have explored higher-order and more complex compensation networks [50, 80, 81], such as the double side LCC compensation widely used in wireless charging for electric vehicles [82]. However, the use of numerous capacitors and inductors increases both the size and complexity of the system. Therefore, a trade-off between optimal output characteristics and network simplicity is necessary. In the following section, we will introduce the LCC-S compensation topology [19, 28, 42, 83]:

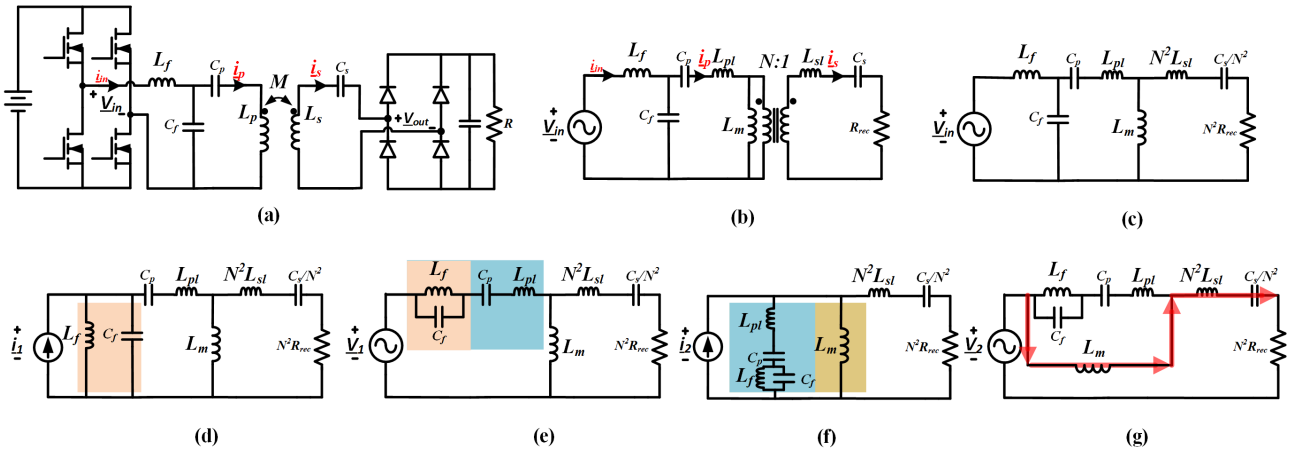

Figure 4.2: Equivalent Circuit of LCC-S.

As shown in Fig. 4.2(a), the primary side of this compensation structure consists of a low-pass filter with L_f and C_f to filter out higher-order harmonics, as well as C_p and L_p to adjust the input impedance angle, ensuring ZVS operation across the entire load variation range. The secondary side is composed of L_s and the compensation capacitor C_s:

$$\omega_r = \frac{1}{\sqrt{L_f C_f}} = \frac{1}{\sqrt{L_s C_s}}. \tag{4.1}$$

The equivalent Cantilever model of circuit in Fig. 4.2 (a) is shown in Fig. 4.2 (b), where $N = \sqrt{\frac{L_p}{L_s}}$, $L_m = N \cdot M$, $L_{pl} = L_p - L_m$, and $L_{sl} = L_s - \frac{L_m}{N^2}$. The rectifier diodes and load resistance can be equivalently represented as a resistance R_{rec}, and the secondary side components are transformed to the primary side as shown in Fig. 4.2 (c).

According to Thevenin's theorem, the voltage source $\underline{V}_{\text{in}}$ and L_f can be equivalently represented as a current source $\underline{i}_1$ with parallel resistance L_f, as shown in Fig. 4.2 (d). Then, applying Norton's theorem, the current source $\underline{i}_1$ and parallel resistance $L_f \parallel C_f$ can be equivalently represented as a voltage source $\underline{V}_1$ with series resistance $L_f \parallel C_f$, as depicted in Fig. 4.2 (e).

Next, according to Thevenin's theorem, the voltage source $\underline{V}_1$ with series resistance $(L_f \parallel C_f) + C_p + L_{pl}$ can be equivalently represented as a current source $\underline{i}_2$ with parallel resistance $(L_f \parallel C_f) + C_p + L_{pl}$, as shown in Fig. 4.2 (f). Finally, applying Norton's theorem, the current source $\underline{i}_2$ and $[(L_f \parallel C_f) + C_p + L_{pl}] \parallel L_m$ can be equivalently represented as a voltage source $\underline{V}_2$ with series resistance $[(L_f \parallel C_f) + C_p + L_{pl}] \parallel L_m$, as shown in Fig. 4.2 (g).

Since L_f and C_f are in parallel resonance, they can be considered an open circuit, and the current will only flow through $L_m + N^2 L_{sl} + \frac{C_s}{N^2}$ to the load. The series resonance of $L_m + N^2 L_{sl}$ with $\frac{C_s}{N^2}$ can be considered a short circuit, consisting a load independent voltage (CV) behaviour, and the resonance condition is independent of the coupling coefficient, unlike $\omega_H = \frac{\omega_r}{\sqrt{1-k}}$ in the SS-CV. This means that even if the relative position of the coils changes, the resonance frequency will remain unchanged, providing better stability compared to the SS-CV configuration.

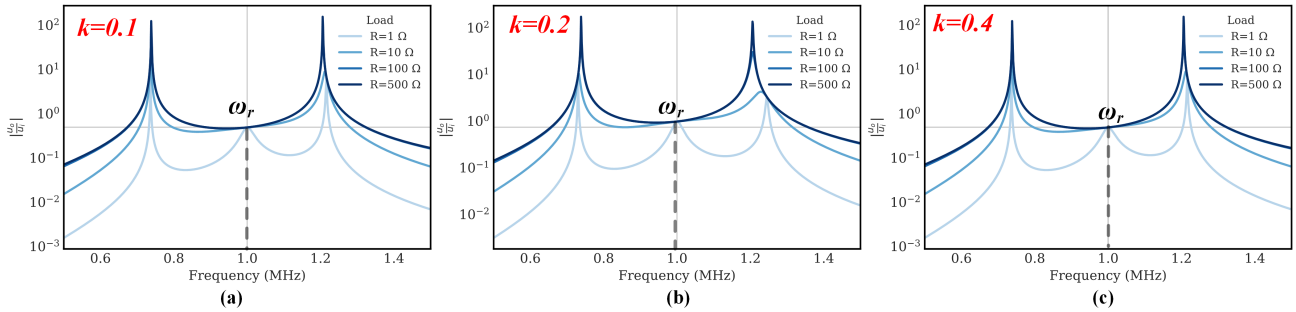

Figure 4.3: LCC-S-Constant Voltage output behaviour at different k.

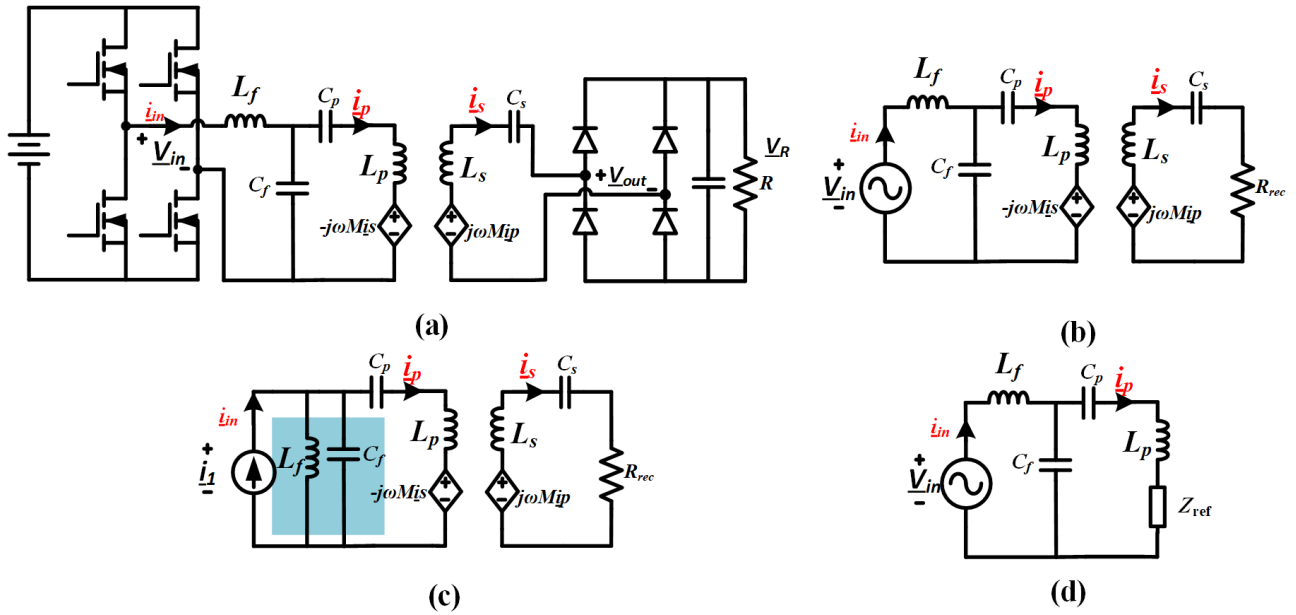

Figure 4.4: Two-port transformer equivalent circuit of LCC-S.

At the same time, we present the Two-port transformer equivalent circuit of the LCC-S topology, as shown in Fig. 4.4 (a). The rectified circuit is equivalently represented as a resistance R_{rec}, as shown in Fig. 4.4 (b). According to Thevenin's theorem, the voltage source $\underline{V}_{\text{in}}$ and series inductance L_f can be equivalently represented as a current source $\underline{i}_1 = \frac{\underline{V}_{\text{in}}}{j\omega_r L_f}$ with parallel inductance L_f, as shown in Fig. 4.4 (c).

Since L_f and C_f are in parallel resonance and can be considered an open circuit, $\underline{i}_p = \underline{i}_1 = \frac{\underline{V}_{\text{in}}}{j\omega_r L_f}$. The secondary side L_s and C_s are in series resonance, effectively shorting the circuit. The controlled voltage source $j\omega_r M \underline{i}_p = j\omega_r M \frac{\underline{V}_{\text{in}}}{j\omega_r L_f} = \frac{M \underline{V}_{\text{in}}}{L_f}$ is entirely applied on the resistance R_{rec}. Therefore, the voltage ratio is given by:

$$\frac{|\underline{V}_{R_{rec}}|}{|\underline{V}_{\text{in}}|} = \frac{M}{L_f} = k \cdot \frac{\sqrt{L_p L_s}}{L_f}. \tag{4.2}$$

Additionally, by transforming the primary controlled voltage source $-j\omega_r M \underline{i}_s$ into an equivalent reflected resistance from the secondary side as shown in Fig. 4.4 (d), we can calculate the equivalent input impedance $\underline{Z}_{\text{in}}$ of $\underline{V}_{\text{in}}$. Using this impedance, we can then design the appropriate value of C_p to achieve ZVS across the entire load range.

In summary, we introduced the principles of the LCC-S compensation topology above, and it is evident that it offers the following advantages:

1. At the resonance frequency ω_r, it exhibits load-independent voltage characteristics:

$$\frac{|\underline{V}_{R\text{rec}}|}{|\underline{V}_{\text{in}}|} = k \cdot \frac{\sqrt{L_p L_s}}{L_f},$$

(In the SS-CV topology has $G_v(\omega_H) = \sqrt{\frac{L_s}{L_p}}$).

2. The resonance frequency $\omega_r = \frac{1}{\sqrt{L_f C_f}} = \frac{1}{\sqrt{L_s C_s}}$ is independent of the coupling conditions (unlike the SS-CV topology, where $\omega_H = \frac{\omega_r}{\sqrt{1-k}}$).

3. At this resonance frequency ω_r, the input impedance phase can be adjusted by tuning the value of C_p, enabling ZVS operation (In the SS-CC topology, the input phase is 0, making it impossible to achieve ZCS or ZVS. In the SS-CV topology, ω_H is too inductive and ω_L is too capacitive, both affecting efficiency).

4. The primary coil current $\underline{i}_p$ remains constant, even when there are multiple receiving coils, making it immune to interference.

4.2 Input Impedance Equivalent Model of CW-VM

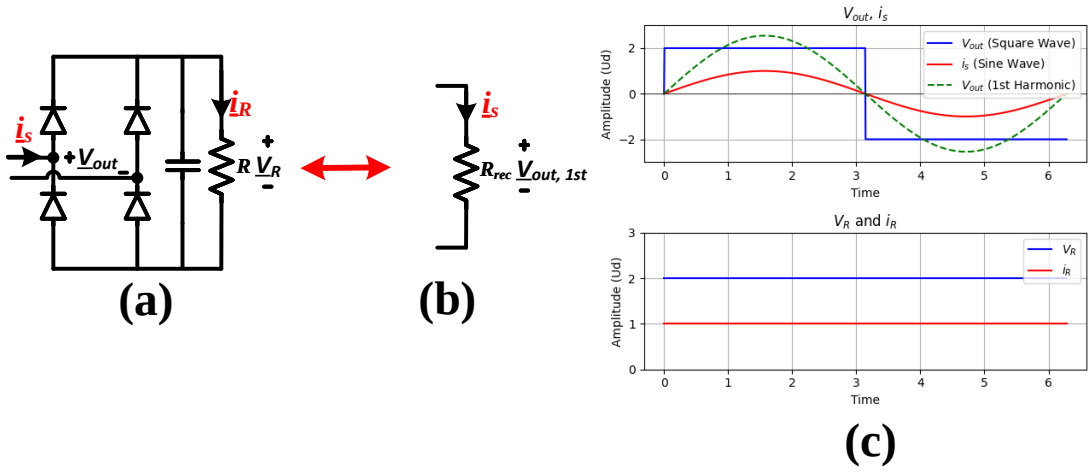

Figure 4.5: Input Equivalent Model of Full Wave Rectifiers.

In the previous descriptions, we have treated the full-wave rectifier circuit, as shown in Fig. 4.5 (a), as an equivalent pure resistance, as shown in Fig. 4.5 (b). Here, $\underline{V}_{\text{out}}$ is a square wave with an amplitude of U_d, and the current flowing into the rectifier $\underline{i}_s$ is a sine wave. The voltage $\underline{V}_R$ across the resistor R is a DC voltage of magnitude U_d, and the current through R is also DC. When we equivalently represent the circuit as in Fig. 4.5 (b), we assume that only the first harmonic of $\underline{V}_{\text{out}}$ is transmitting energy (considering the high-quality factor of the coil). According to Fourier decomposition:

$$\underline{V}_{\text{out, 1st}} = \frac{4U_d}{\pi}\sin(\omega t), \tag{4.3}$$

The RMS value of $\underline{V}_{\text{out, 1st}}$ is:

$$\text{RMS}(\underline{V}_{\text{out, 1st}}) = \frac{2\sqrt{2}U_d}{\pi}, \tag{4.4}$$

According to the principle of energy conservation:

$$\left(\frac{2\sqrt{2}U_d}{\pi}\right)^2 \Big/ R_{\text{rec}} = \frac{U_d^2}{R}, \tag{4.5}$$

Thus, the equivalent resistance R_{rec} is:

$$R_{\text{rec}} = \frac{8R}{\pi^2}. \tag{4.6}$$

The FHA method generally provides good accuracy in most cases [43, 44, 84, 85]. However, as the frequency increases, the rectified voltage will lag behind the rectified current because the commutation of the diodes is affected by the parasitic capacitance of the diodes, making the load appear capacitive. This will affect the input impedance of the voltage source. To achieve a more accurate equivalent model, a method of paralleling a capacitance with the resistance has been proposed, which offers better precision [19, 26, 86]. Alternatively, by utilizing a parallel capacitance C_p, the circuit can be equivalently modeled as a resistor in series with a capacitance, offering greater simplicity [87–89]. Using more precise analytical methods [90, 91] or scanning the load parameter characteristics [92, 93] can provide a more accurate model, but this significantly increases the workload.

For the Cockcroft-Walton Voltage Multiplier, at lower orders and frequencies, the parasitic capacitance of the diodes can be neglected, allowing the circuit to be equivalently modeled as a pure resistance [94, 95]. For higher orders and higher frequencies, several equivalent circuits have been proposed. Some are based on simple equivalence [96], others require the inclusion of a parallel capacitance C_p [75], and some are based on the assumption that the circuit reaches steady state with a very short discharge time [97–100]. To establish an equivalent input model for the CW VM suitable for charging capacitors, we will analyze its operating modes and develop the corresponding models.

As shown in Fig. 4.6, this is the proposed circuit structure. A DC voltage is converted into a square wave with an amplitude of V_{in} using a full-bridge inverter, which then drives the LCC-S lossy coupled transformer. On the output side, a sinusoidal waveform is generated to feed the CW-VM, which multiplies the low-voltage AC input to a DC output to charge the capacitor C_{load}. Here, R represents the 10 MΩ resistance of the voltage probe. In 3.1.2, we introduced the current mode of the CW, but we neglected the junction capacitance of the Schottky diodes. In reality, each diode has a nonlinear parasitic capacitance [100], as shown in Fig. 4.7, which affects the current mode as follows:

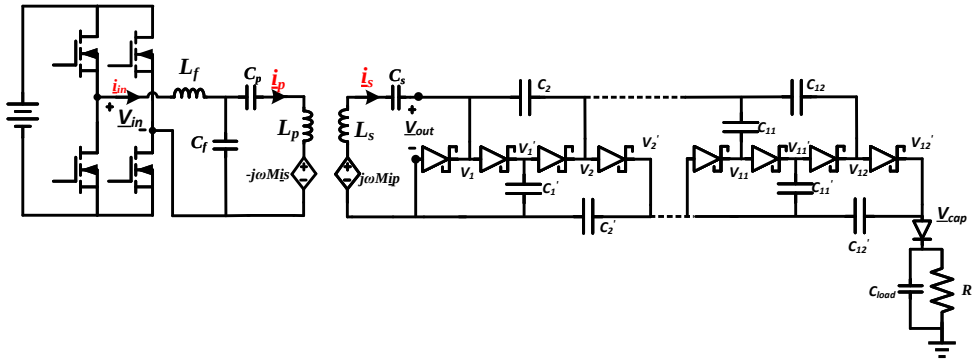

Figure 4.6: Proposed LCC-S power CW-VM Circuit.

1. **Mode 1**: All diodes are blocked, and the current flows through the junction capacitors of the diodes. Reverse voltages shift from V_{in} to $-V_{\text{in}}$.

2. **Mode 2**: As described earlier in 3.1.2, the odd-numbered diodes conduct sequentially from the highest stage to the lowest stage.

3. **Mode 3**: The same sequence occurs during the negative half-cycle.

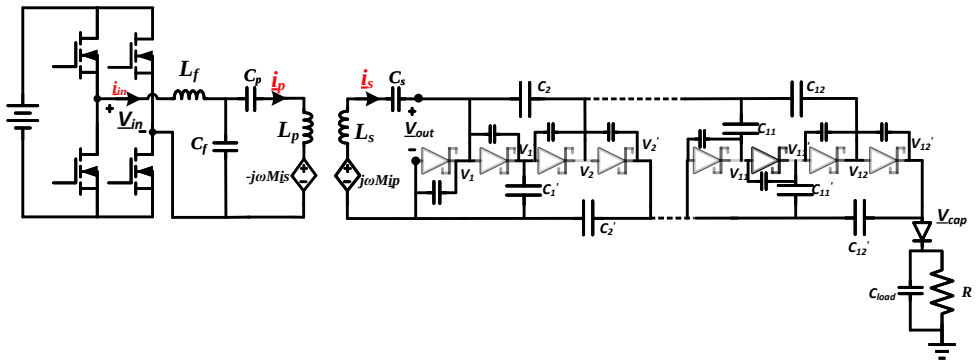

Figure 4.7: Proposed LCC-S power CW-VM Circuit considering the junction capacitance of the diode.

At the same time, the capacitive load can be equivalently modeled as a resistor with a continuously varying value and a capacitor (causing the voltage to lag behind the current). However, quantifying this capacitance is very

complex, and no method has been found in the literature, indicating a need for further research. Additionally, the junction capacitance of the diodes requires a voltage change every cycle, so the overall CW input impedance can be modeled as a capacitor C_k and a varying resistor R, where $C_k = 2nC_d + C_c$, with C_d (=43 pF) representing the diode parasitic capacitance and C_c representing the equivalent capacitance of the charging capacitor, as shown in Fig. 4.8.

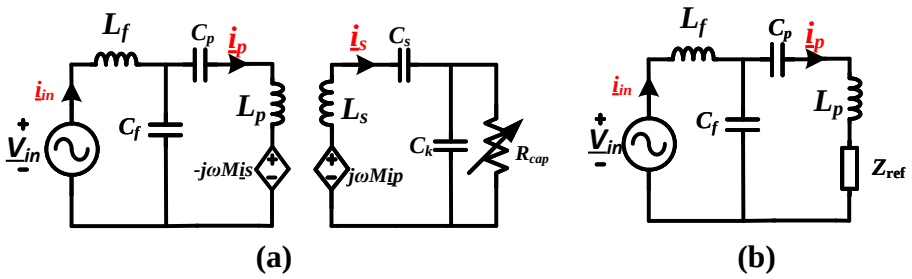

Figure 4.8: Proposed LCC-S power CW-VM Circuit considering the junction capacitance of the diode.

To realize ZVS, the turn-off current must be able to fully discharge the equivalent junction capacitor (C_{oss}) of the switching devices during the dead-time period (t_d):

$$Q = \int_0^{t_d} i_{\text{off}}(t)dt \geq 2C_{\text{oss}}V_{\text{in}} \tag{9}$$

$$\mathbf{Z_f} = \frac{\frac{L_f}{C_f}}{Z'_{\text{ref}} + j\left(\omega_r L_p - \frac{1}{\omega_r C_p} - \frac{1}{\omega_r C_f}\right)}, \tag{4.7}$$

Through calculation, we obtained the following system parameters:

Table 4.1: Specifications of the WPT System

Specifications	**Symbol**	**Practical Value**
Input voltage	V_{in}	17 V
Output voltage	V_{cap}	330 V
Switching frequency	f_{r}	1 MHz
Transmitter coil self-inductance	L_p	4.84μH
Transmitter coil resistance	R_p	0.25Ω
Receiver coil self-inductance	L_s	4.73μH
Receiver coil resistance	R_s	0.25Ω
Coupling coefficient range	k	0.174

Table 4.2: Passive Components Value in the LCC-S Circuit

Component	**Practical Value**
L_f	1 μH
C_f	25.3 nF
C_p	6.55 nF
C_s	5.37 nF

4.3 Experiment Verification

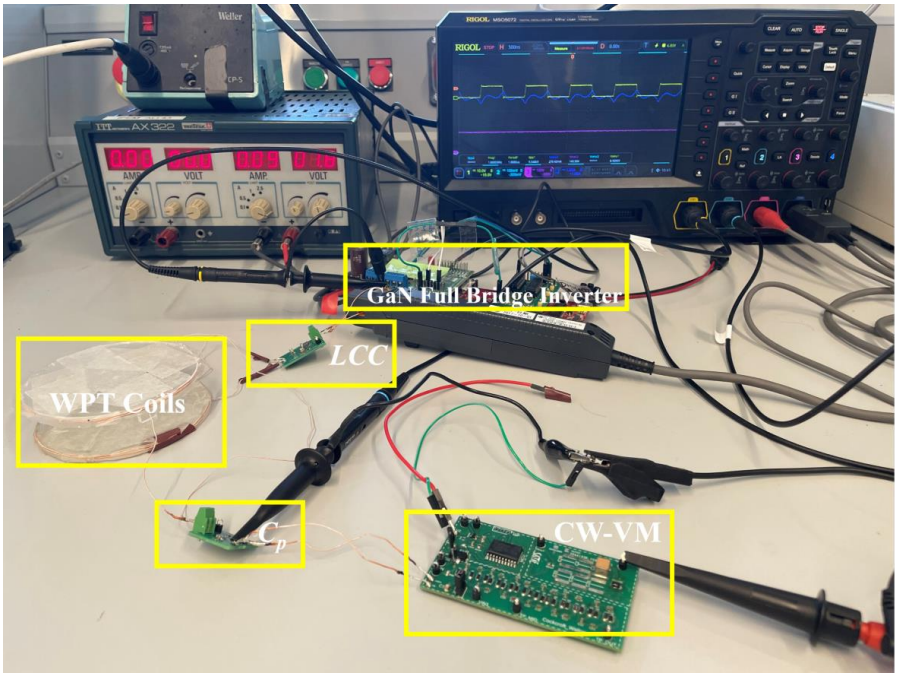

Figure 4.9: The picture of the experiment setup.

The experimental setup is shown in Fig. 4.9. We control the LMG5200 GaN MOSFET using the LAUNCHXL-F28377 to generate a 200 ms, 1 MHz burst, after which it is turned off for 2.3 seconds. During this off period, the voltage across the capacitor rapidly decreases through the 10 MΩ resistor of the voltage probe. By operating cyclically in this manner, the voltage across the capacitor will periodically rise from 300V to 330V (in 200 ms) and then drop from 330V to 300V (in 2.3 seconds). This setup simulates the operation of the Marx Modulator [18].

As shown in the oscilloscope results in Fig. 4.10 (a) and (b), $\underline{V}_{cap}$ periodically varies from 300 V to 330 V. In Fig. 4.10 (c), observed over a shorter time frame, $\underline{V}_{in}$ is a square wave, while $\underline{i}_{in}$, which includes multiple harmonics, does not appear purely sinusoidal. However, it is evident that $\underline{i}_{in}$ lags behind $\underline{V}_{cap}$, indicating that ZVS is achieved. The lagging current helps to discharge the charge on the GaN MOSFET's C_{oss}, thus enabling zero turn-on loss. In Fig. 4.10 (d), it can be observed that $\underline{i}_s$ leads $\underline{V}_{out}$, confirming that the overall CW input impedance exhibits capacitive behavior.

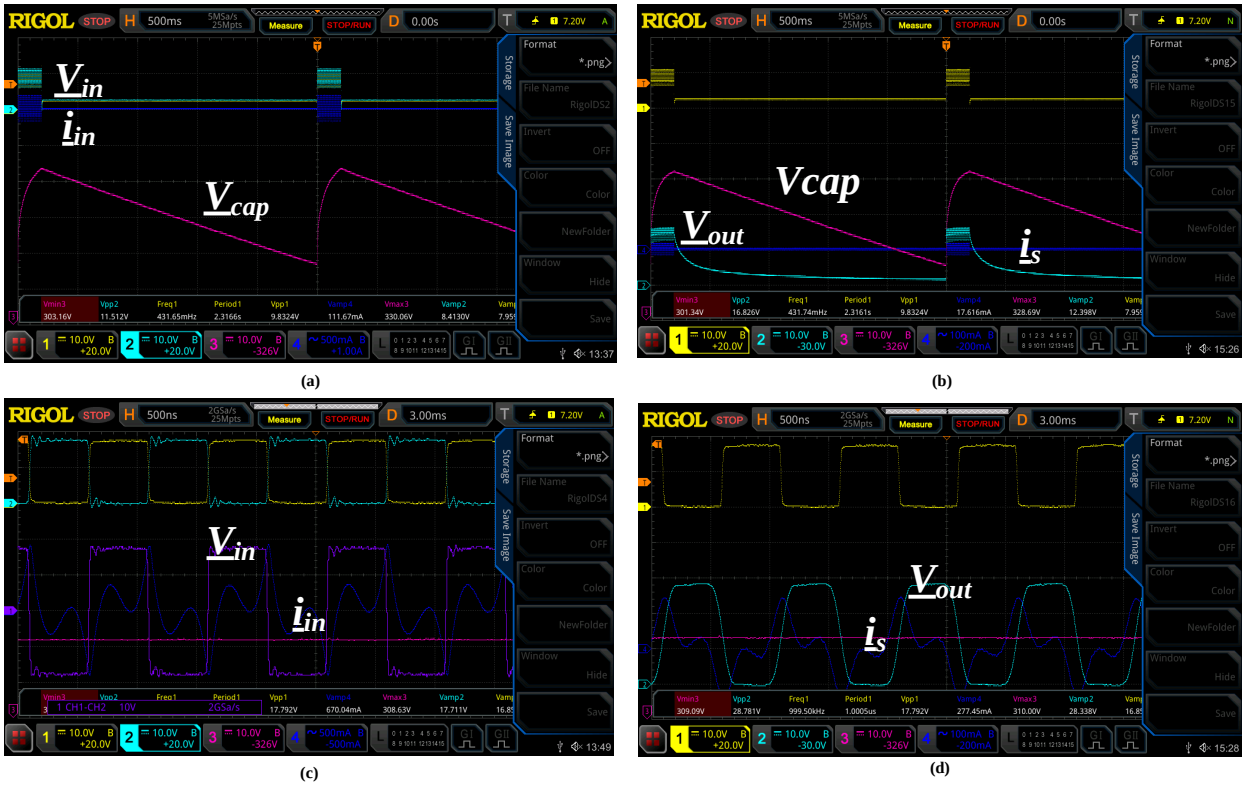

Figure 4.10: (a,c) The experiment $\underline{V}_{in}$, $\underline{i}_{in}$, and $\underline{V}_{cap}$ waveform. (b,d) The experiment $\underline{V}_{out}$, $\underline{i}_{s}$ and $\underline{V}_{cap}$ waveform.

By calculating the input and output power of the system, we can determine the system's efficiency.

When charging the capacitor from 0 V to 180 V:

The input energy of the WPT system is 24.359 mJ, with magnetic losses in the coil amounting to 0.012 mJ, transmitter coil resistance losses of 3.1801 mJ, and receiver coil losses of 1.7702 mJ. The energy input to the CW circuit is 19.1588 mJ.

The energy input to the CW circuit is 19.1588 mJ, with diode losses of 0.6298 mJ and capacitor losses of 2.234 mJ. The load capacitor receives 16.295 mJ of energy.

the efficiency of the WPT system is 78.65%, and the efficiency of the CW circuit is 85.05%, the overall is 66.89%.

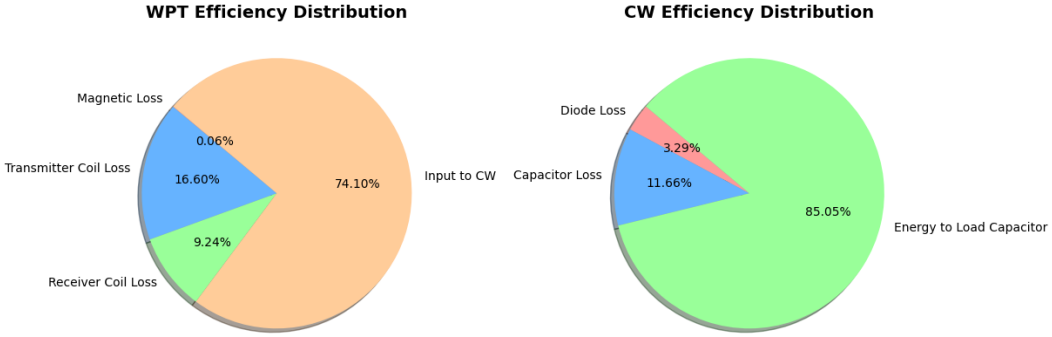

Figure 4.11: Efficiency Distribution of WPT and CW when charging C_{load} from 0-180 V.

When charging the capacitor from 300 V to 330 V:

The input energy of the WPT system is 24.845 mJ, with transmitter coil resistance losses of 14.351 mJ, and receiver coil losses of 0.053 mJ. The output energy is 10.329 mJ.

The energy input to the CW circuit is 10.329 mJ, with diode losses of 0.245 mJ and capacitor losses of 0.5266 mJ. The load capacitor receives 9.5574 mJ of energy.

the efficiency of the WPT system is 41.57%, and the efficiency of the CW circuit is 92.8%, the overall is 38.57%. Additionally, the hard switch loss eliminated by ZVS is approximately 15.36 mJ, highlighting the necessity of implementing ZVS in the system.

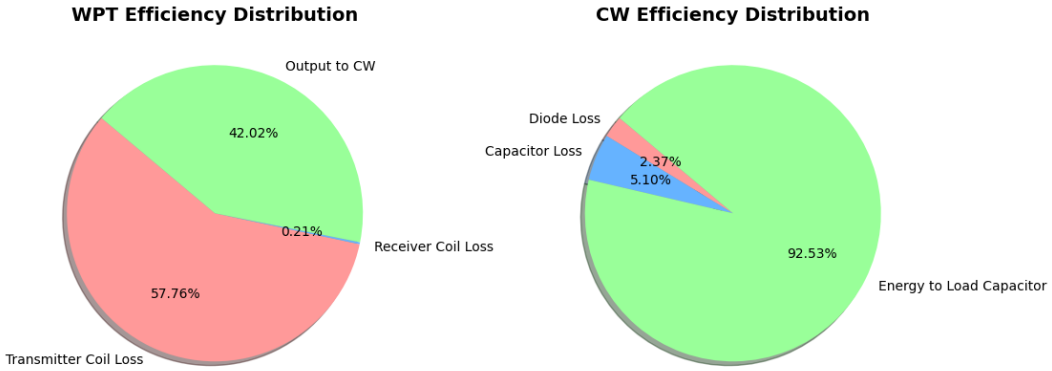

Figure 4.12: Efficiency Distribution of WPT and CW when charging C_{load} from 300-330 V.

From the analysis of the efficiency during different stages of capacitor charging, we observed that the WPT efficiency is higher when charging at lower capacitor voltages. This is because, at low voltage, the capacitor behaves as a low-value resistor, which is reflected back to the primary side as a high resistance (refer 2.1.1). As a result, most of the voltage is dropped across this reflected resistance, with the primary coil's parasitic resistance contributing only a small portion, leading to relatively high WPT efficiency. However, due to the low equivalent resistance of the capacitor, the output current of the CW circuit is relatively high, causing significant losses in the diode and the ESR of the capacitors, thus resulting in relatively lower CW efficiency.

Conversely, when charging at higher capacitor voltages, the capacitor behaves as a high-value resistor, which is reflected back to the primary side as a low resistance. Consequently, most of the voltage is dropped across the primary coil's parasitic resistance, leading to low WPT efficiency. However, due to the high equivalent resistance of the capacitor, the output current of the CW circuit is relatively low, resulting in lower diode and capacitor ESR losses, and thus higher CW efficiency.

Chapter 5

Conclusions and Perspectives

5.1 Conclusions

In this thesis, our objective was to design the WPT component for a DEAA system, which required a WPT system capable of generating a 330V high-voltage output for charging capacitors. At the outset, we reviewed and introduced four classic compensation topologies, attempting to address the challenge using simple SS-CC or SS-CV methods. However, simulations revealed that these approaches either led to excessive current and magnetic fields in the transmitting coil or required large and densely wound coils on the receiving side, which increased secondary-side losses and led to unstable coupling. Consequently, we shifted our focus to the Cockcroft-Walton (CW) voltage multiplier, a circuit that can step up an AC voltage to a high-voltage DC output.

In Chapter 3, we briefly introduced the principles of the CW circuit and its internal operation modes. We then optimized the parameters to select suitable components, balancing performance, size, and losses. The results from both calculations and simulations indicated that the designed CW circuit achieved high efficiency.

In Chapter 4, we introduced a novel WPT compensation structure, which demonstrated better resilience to coupling variations compared to the SS topology. We combined the LCC-S topology with the CW circuit and, through analyzing the CW operating modes, proposed a method for determining the equivalent input impedance of the CW circuit. This provided a simpler approach for designing the compensation structure. Using this equivalent circuit, we subsequently designed and experimented with an LCC-S Based WPT Powering VM for High Voltage Capacitor Charging system. The experimental results showed good alignment with our design expectations.

5.2 Perspectives

To improve the efficiency of the system, the simplest and most direct approach is to reduce the internal resistance of the WPT coils. As shown in Fig. 2.10, by increasing the coil quality factor, the efficiency is enhanced across the entire

load range. Additionally, we can design the system parameters so that the WPT operates with higher efficiency within the equivalent load range while charging the capacitor (300V-330V). Another approach could involve using variable capacitance [101], active rectification [102,103], or circuits such as cascode buck-boost to adjust the equivalent load or optimal efficiency point [44], thereby ensuring that the system always operates at its highest efficiency. However, these methods would require additional components and detection algorithms, which would increase the system's size.

For example, if we design both the transmitting and receiving coils to have an inductance of 16 μH and an internal resistance of 0.2 Ω, then through simulation:

When charging the capacitor from 300 V to 330 V:
The input energy of the WPT system is 11.69 mJ, with transmitter coil resistance losses of 1.054 mJ, and receiver coil losses of 0.044 mJ. The output energy is 10.47 mJ.

The energy input to the CW circuit is 10.47 mJ, with diode losses of 0.345 mJ and capacitor losses of 0.395 mJ. The load capacitor receives 9.73 mJ of energy.

the efficiency of the WPT system is 89.56%, and the efficiency of the CW circuit is 92.9%, the overall is 83.2%.

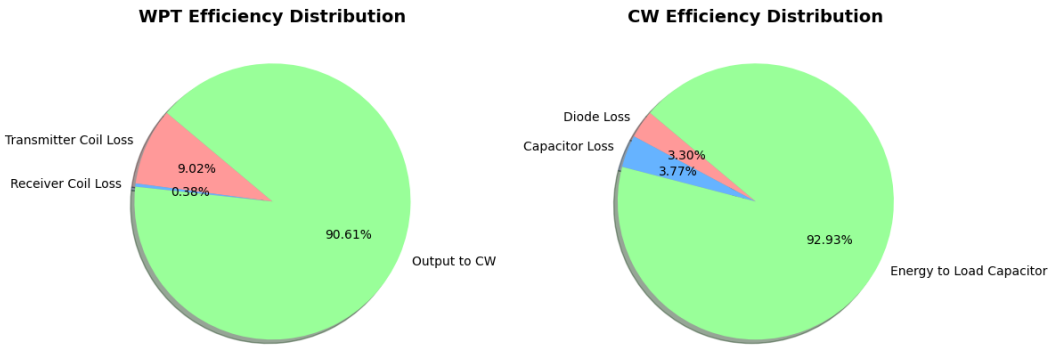

Figure 5.1: Efficiency Distribution of WPT and CW when charging C_{load} from 300-330 V With Bigger Q Value of Coil.

In addition to the CW circuit requiring energy transmission via WPT, we also need to simultaneously supply energy to 24 smaller coils, each of which transmits power to a control MCU. These MCUs are responsible for receiving ASK-modulated signals and controlling the operation and stopping of the CW circuit and the Marx Modulator [18]. These 24 coils should be placed closely together with the CW coil to minimize the coil area, which means there will be mutual coupling between them, as shown in the Fig. 5.2. Therefore, we can describe this system using the following Equ. 5.1, the mutual coupling between any pair of receiving coils can be considered as strong coupling, with a coupling coefficient $k = 1$.

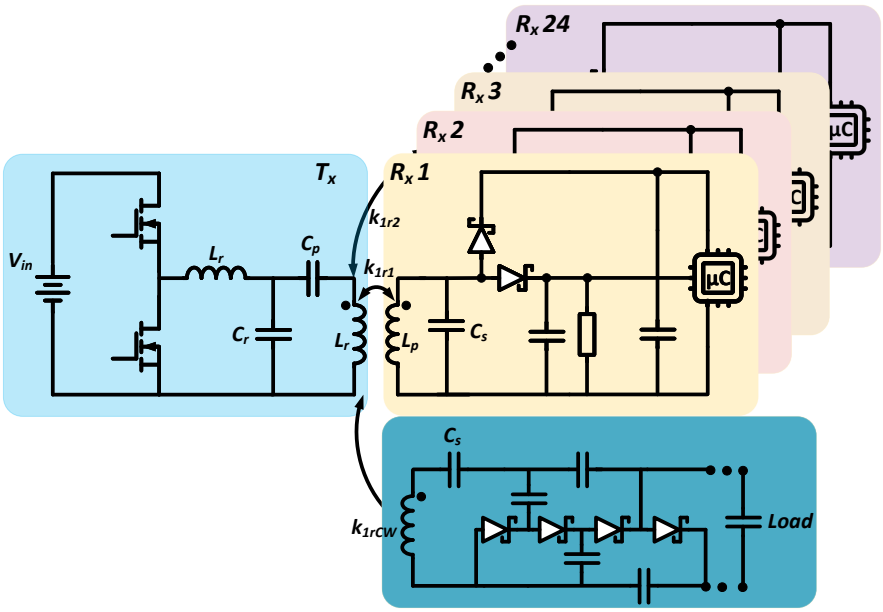

Figure 5.2: Wireless Power Transfer for Multiple Receivers.

$$\begin{bmatrix} V_{\text{IN}} \\ 0 \\ \vdots \\ 0 \\ 0 \end{bmatrix} = \begin{bmatrix} R_t & j\omega M_{t1} & \cdots & j\omega M_{t(n-1)} & j\omega M_{tn} \\ j\omega M_{t1} & R_1 + Z_{L1} & \cdots & j\omega M_{1(n-1)} & j\omega M_{1n} \\ \vdots & \vdots & \ddots & \vdots & \vdots \\ j\omega M_{t(n-1)} & j\omega M_{1(n-1)} & \cdots & R_{n-1} + Z_{L(n-1)} & j\omega M_{(n-1)n} \\ j\omega M_{tn} & j\omega M_{1n} & \cdots & j\omega M_{(n-1)n} & R_n + Z_{Ln} \end{bmatrix} \begin{bmatrix} I_t \\ I_1 \\ \vdots \\ I_{n-1} \\ I_n \end{bmatrix} \tag{5.1}$$

Previously, some research has addressed one-to-many WPT transmission; however, these studies either neglect the mutual coupling between multiple receiving coils [19, 104] or consider only specific coupling scenarios [105]. The case where the receiving coils are strongly coupled to each other has not yet been thoroughly investigated. Therefore, further research is needed to determine how these 24 small receiving coils can work together with the CW receiving coil.

In addition, the design of the shielding layer for the transmitting coil, the SAR (Specific Absorption Rate) limitations for the receiving coils [27], and the overall heating issues of the device all require further research.

Optimisation of Wireless Power Transfer for a Dielectric Elastomer Augmented Aorta

Yiming Wei [1,2], *Guojun Lan* [1,2], *Christophe Baron* [1,2] *and Morgan Almanza* [1,2]

[1]*Université Paris-Saclay, ENS Paris-Saclay, CNRS, SATIE*
[2]*École polytechnique fédérale de Lausanne (EPFL), Integrated Actuators Laboratory*

Context

This M2 internship, under the direction of Morgan Almanza, optimises the power electronics and the wireless transmission part of this medical device, with the aim of making it **more compact, safe and efficient**.

Principle of Cardiac Assist Device

What is Dielectric elastomer actuator (DEA):
Two layers of flexible electrodes sandwich a flexible dielectric elastomer. When high voltage is applied, a strong electric field compresses the elastomer.

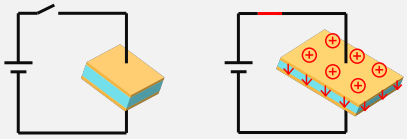

What is Dielectric Elastomer Augmented Aorta (DEAA):
The tubular DEA modulates its stiffness to coincide with the heart's cycle [1]:

(1) stiffening at 0 V during diastole to support aortic recoil, promoting the continuous flow of blood
(2) softening at 7 kV during systole to facilitate aortic expansion.

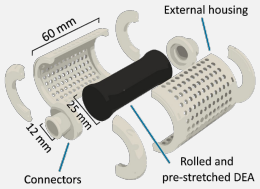

(a) DEAA design. Reprinted from [2].

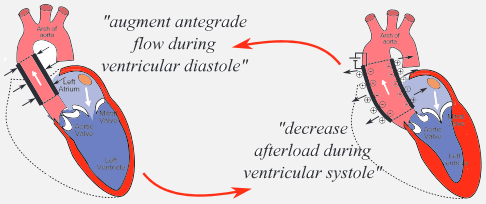

(b) DEAA working cycle. Reprinted from [1].

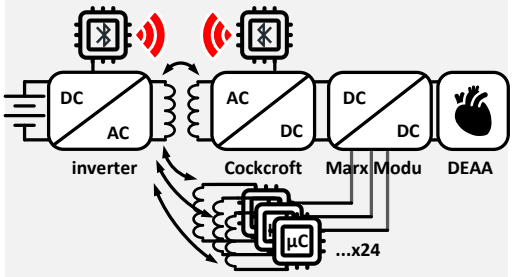

(c) DEAA electronic system.

Wireless Power Transfer for One Receiver

In order to increase the power transfer capability and reduce the coil area, we need a compensation network to cancel the leakage inductance of the coil.

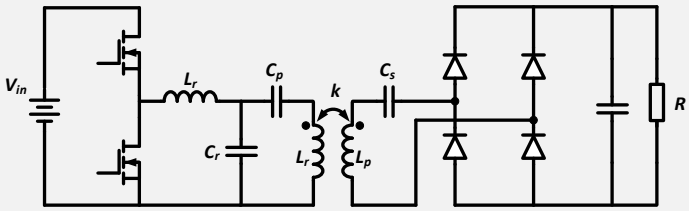

LCCL-LC Resonant Converter [4] :

(1) coupling independent resonant frequency
(2) load-independent output voltage
(3) load independent transmitter coil current
(4) inductive reflected impedance for ZVS

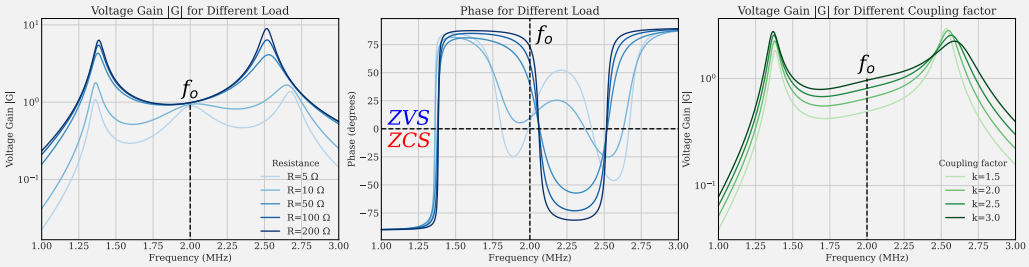

Wireless Power Transfer for Multiple Receivers

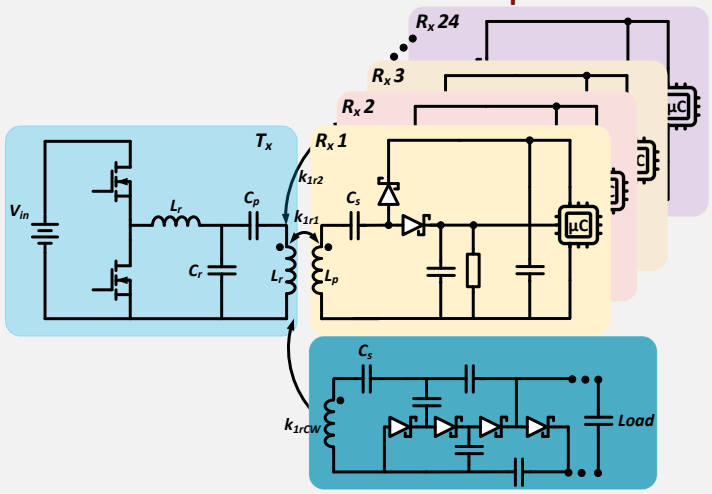

$$\begin{bmatrix} \mathbf{V_{IN}} \\ 0 \\ \vdots \\ 0 \\ 0 \end{bmatrix} = \begin{bmatrix} R_t & j\omega M_{t1} & \cdots & j\omega M_{t(n-1)} & j\omega M_{tn} \\ j\omega M_{t1} & R_1 + \mathbf{Z_{L1}} & \cdots & j\omega M_{1(n-1)} & j\omega M_{1n} \\ \vdots & \vdots & \ddots & \vdots & \vdots \\ j\omega M_{t(n-1)} & j\omega M_{1(n-1)} & \cdots & R_{n-1} + \mathbf{Z_{L(n-1)}} & j\omega M_{(n-1)n} \\ j\omega M_{tn} & j\omega M_{1n} & \cdots & j\omega M_{(n-1)n} & R_n + \mathbf{Z_{Ln}} \end{bmatrix} \begin{bmatrix} \mathbf{I_t} \\ \mathbf{I_1} \\ \vdots \\ \mathbf{I_{n-1}} \\ \mathbf{I_n} \end{bmatrix}$$

References:

[1] M. Almanza, F. Clavica, J. Chavanne, *et al. Advanced science*, 2021, 8(6): 2001974.
[2] S. E. Jahren, T. Martinez, A. Walter, *et al. Interdisciplinary cardiovascular and thoracic surgery*, 2024, 38(3): ivae027.
[3] M. Almanza, T. Martinez, M. Petit, *et al. IEEE Transactions on Power Electronics*, 2022, 37(11): 13014-13021.
[4] J. Feng, Q. Li, F. C. Lee, *et al. IEEE Transactions on Power Electronics*, 2020, 36(4): 3828-3839.

Bibliography

[1] B. Shahim, C. J. Kapelios, G. Savarese, and L. H. Lund, "Global public health burden of heart failure: an updated review," *Cardiac Failure Review*, vol. 9, 2023.

[2] P. M. Becher, L. H. Lund, A. J. Coats, and G. Savarese, "An update on global epidemiology in heart failure," 2022.

[3] N. L. Bragazzi, W. Zhong, J. Shu, A. Abu Much, D. Lotan, A. Grupper, A. Younis, and H. Dai, "Burden of heart failure and underlying causes in 195 countries and territories from 1990 to 2017," *European Journal of Preventive Cardiology*, vol. 28, no. 15, pp. 1682–1690, 2021.

[4] T. Puehler, S. Ensminger, M. Schoenbrodt, J. Börgermann, E. Rehn, K. Hakim-Meibodi, M. Morshuis, and J. Gummert, "Mechanical circulatory support devices as destination therapy—current evidence," *Annals of cardiothoracic surgery*, vol. 3, no. 5, p. 513, 2014.

[5] J. D. Dedhia, K. R. N. Chakravarthy, and A. B. Ahmed, "Intra aortic balloon pump (iabp): past, present and future," *Indian Journal of Anaesthesia*, vol. 52, no. 4, pp. 387–396, 2008.

[6] M. Almanza, F. Clavica, J. Chavanne, D. Moser, D. Obrist, T. Carrel, Y. Civet, and Y. Perriard, "Feasibility of a dielectric elastomer augmented aorta," *Advanced science*, vol. 8, no. 6, p. 2001974, 2021.

[7] R. Pelrine, R. Kornbluh, J. Joseph, R. Heydt, Q. Pei, and S. Chiba, "High-field deformation of elastomeric dielectrics for actuators," *Materials Science and Engineering: C*, vol. 11, no. 2, pp. 89–100, 2000.

[8] A. Benouhiba, A. Walter, S. E. Jahren, T. Martinez, F. Clavica, D. Obrist, Y. Civet, and Y. Perriard, "Dielectric elastomer actuator-based valveless impedance-driven pumping for meso-and macroscale applications," *Soft robotics*, vol. 11, no. 2, pp. 198–206, 2024.

[9] X. Ji, X. Liu, V. Cacucciolo, M. Imboden, Y. Civet, A. El Haitami, S. Cantin, Y. Perriard, and H. Shea, "An autonomous untethered fast soft robotic insect driven by low-voltage dielectric elastomer actuators," *Science Robotics*, vol. 4, no. 37, p. eaaz6451, 2019.

[10] Q. De Menech, S. Zammouri, S. Konstantinidi, A. Benouhiba, Y. Civet, and Y. Perriard, "An artificial urinary sphincter based on dielectric elastomer technology," in *Electroactive Polymer Actuators and Devices (EAPAD) XXVI*, vol. 12945. SPIE, 2024, pp. 28–33.

[11] S. Konstantinidi, C. Imholz, T. Martinez, A. Benouhiba, A. Walter, Y. Civet, N. Lindenblatt, and Y. Perriard, "Real-time actuation of a dielectric elastomer actuator neuroprosthesis for facial paralysis," *Smart Materials in Medicine*, vol. 5, pp. 15–23, 2024.

[12] S. Konstantinidi, Q. De Menech, T. Martinez, P. Germano, A. Boegli, Y. Civet, and Y. Perriard, "Inversing the actuation cycle of dielectric elastomer actuators for a facial prosthesis," in *Electroactive Polymer Actuators and Devices (EAPAD) XXVI*, vol. 12945. SPIE, 2024, pp. 276–282.

[13] S. E. Jahren, T. Martinez, A. Walter, F. Clavica, P. P. Heinisch, E. Buffle, M. M. Luedi, J. Hörer, D. Obrist, T. Carrel *et al.*, "Novel para-aortic cardiac assistance using a pre-stretched dielectric elastomer actuator," *Interdisciplinary cardiovascular and thoracic surgery*, vol. 38, no. 3, p. ivae027, 2024.

[14] T. Martinez, S. E. Jahren, A. Walter, J. Chavanne, F. Clavica, L. Ferrari, P. P. Heinisch, D. Casoni, A. Haeberlin, M. M. Luedi *et al.*, "A novel soft cardiac assist device based on a dielectric elastomer augmented aorta: An in vivo study," *Bioengineering & translational medicine*, vol. 8, no. 2, p. e10396, 2023.

[15] S. E. Jahren, T. Martinez, A. Walter, L. Ferrari, F. Clavica, D. Obrist, Y. Civet, and Y. Perriard, "Hemodynamic effects of a dielectric elastomer augmented aorta on aortic wave intensity: An in-vivo study," *Journal of biomechanics*, vol. 159, p. 111777, 2023.

[16] L. Pniak, M. Almanza, Y. Civet, and Y. Perriard, "Ultrahigh-voltage switch for bidirectional dc–dc converter driving dielectric elastomer actuator," *IEEE Transactions on Power Electronics*, vol. 35, no. 12, pp. 13 172–13 181, 2020.

[17] R. Mottet, M. Almanza, L. Pniak, A. Boegli, and Y. Perriard, "Ultra-high-voltage (7-kv) bidirectional flyback converter used to drive capacitive actuators," *IEEE Transactions on Industry Applications*, vol. 57, no. 5, pp. 5145–5156, 2021.

[18] M. Almanza, T. Martinez, M. Petit, Y. Civet, Y. Perriard, and M. LoBue, "Adaptation of a solid-state marx modulator for electroactive polymer," *IEEE Transactions on Power Electronics*, vol. 37, no. 11, pp. 13 014–13 021, 2022.

[19] J. Feng, Q. Li, F. C. Lee, and M. Fu, "Lccl-lc resonant converter and its soft switching realization for omnidirectional wireless power transfer systems," *IEEE Transactions on Power Electronics*, vol. 36, no. 4, pp. 3828–3839, 2020.

[20] S. Li and C. C. Mi, "Wireless power transfer for electric vehicle applications," *IEEE journal of emerging and selected topics in power electronics*, vol. 3, no. 1, pp. 4–17, 2014.

[21] J. H. Kim, B.-S. Lee, J.-H. Lee, S.-H. Lee, C.-B. Park, S.-M. Jung, S.-G. Lee, K.-P. Yi, and J. Baek, "Development of 1-mw inductive power transfer system for a high-speed train," *IEEE Transactions on Industrial Electronics*, vol. 62, no. 10, pp. 6242–6250, 2015.

[22] D. Campoccia, L. Montanaro, and C. R. Arciola, "A review of the clinical implications of anti-infective biomaterials and infection-resistant surfaces," *Biomaterials*, vol. 34, no. 33, pp. 8018–8029, 2013.

[23] G. Gandelman, W. H. Frishman, C. Wiese, V. Green-Gastwirth, S. Hong, W. S. Aronow, and H. W. Horowitz, "Intravascular device infections: epidemiology, diagnosis, and management," *Cardiology in review*, vol. 15, no. 1, pp. 13–23, 2007.

[24] O. Knecht and J. W. Kolar, "Performance evaluation of series-compensated ipt systems for transcutaneous energy transfer," *IEEE Transactions on Power Electronics*, vol. 34, no. 1, pp. 438–451, 2018.

[25] O. M. Knecht, "Transcutaneous energy and information transfer for left ventricular assist devices," Ph.D. dissertation, ETH Zurich, 2017.

[26] O. Knecht, R. Bosshard, and J. W. Kolar, "High-efficiency transcutaneous energy transfer for implantable mechanical heart support systems," *IEEE Transactions on Power Electronics*, vol. 30, no. 11, pp. 6221–6236, 2015.

[27] O. Knecht and J. W. Kolar, "Impact of transcutaneous energy transfer on the electric field and specific absorption rate in the human tissue," in *IECON 2015-41st Annual Conference of the IEEE Industrial Electronics Society*. IEEE, 2015, pp. 004 977–004 983.

[28] C. Xiao, D. Cheng, and K. Wei, "An lcc-c compensated wireless charging system for implantable cardiac pacemakers: Theory, experiment, and safety evaluation," *IEEE Transactions on Power Electronics*, vol. 33, no. 6, pp. 4894–4905, 2017.

[29] G. L. Barbruni, C. Cordara, M. Carminati, S. Carrara, and D. Ghezzi, "A frequency-switching inductive power transfer system for wireless, miniaturised and large-scale neural interfaces," *IEEE Transactions on Biomedical Circuits and Systems*, 2024.

[30] XP Power, "Sf a series," 2017. [Online]. Available: https://www.xppower.com/portals/0/pdfs/SF_A_Series.pdf?ver=2017-02-14-095149-617

[31] J. C. Maxwell, "Viii. a dynamical theory of the electromagnetic field," *Philosophical transactions of the Royal Society of London*, no. 155, pp. 459–512, 1865.

[32] N. Tesla, *High frequency oscillators for electro-therapeutic and other purposes*. Simon and Schuster, 2015.

[33] J. Feng, "6.78 mhz omnidirectional wireless power transfer system for portable devices application," Ph.D. dissertation, Virginia Polytechnic Institute and State University, 2020.

[34] A. Kurs, A. Karalis, R. Moffatt, J. D. Joannopoulos, P. Fisher, and M. Soljacic, "Wireless power transfer via strongly coupled magnetic resonances," *science*, vol. 317, no. 5834, pp. 83–86, 2007.

[35] Y. Wang, Z. Sun, Y. Guan, and D. Xu, "Overview of megahertz wireless power transfer," *Proceedings of the IEEE*, vol. 111, no. 5, pp. 528–554, 2023.

[36] G. L. Barbruni, P. M. Ros, D. Demarchi, S. Carrara, and D. Ghezzi, "Miniaturised wireless power transfer systems for neurostimulation: A review," *IEEE Transactions on Biomedical Circuits and Systems*, vol. 14, no. 6, pp. 1160–1178, 2020.

[37] M. J. Karimi, A. Schmid, and C. Dehollain, "Wireless power and data transmission for implanted devices via inductive links: A systematic review," *IEEE Sensors Journal*, vol. 21, no. 6, pp. 7145–7161, 2021.

[38] Y. Yao, P. Sun, X. Liu, Y. Wang, and D. Xu, "Simultaneous wireless power and data transfer: A comprehensive review," *IEEE Transactions on Power Electronics*, vol. 37, no. 3, pp. 3650–3667, 2021.

[39] A. Adib, K. K. Afridi, M. Amirabadi, F. Fateh, M. Ferdowsi, B. Lehman, L. H. Lewis, B. Mirafzal, M. Saeedifard, M. B. Shadmand *et al.*, "E-mobility—advancements and challenges," *IEEE Access*, vol. 7, pp. 165 226–165 240, 2019.

[40] J. Lee, V. Leung, A.-H. Lee, J. Huang, P. Asbeck, P. P. Mercier, S. Shellhammer, L. Larson, F. Laiwalla, and A. Nurmikko, "Wireless ensembles of sub-mm microimplants communicating as a network near 1 ghz in a neural application," *BioRxiv*, pp. 2020–09, 2020.

[41] Z. Fang, H. Yue, Z. Wei, Z. Zhang, and Z. Huang, "A control-free series resonant converter for battery charging with automatic cc-to-cv profile and whole-process high efficiency," *IEEE Transactions on Power Electronics*, vol. 38, no. 7, pp. 8666–8675, 2023.

[42] S. Li, F. Li, R. Zhang, C. Tao, and L. Wang, "Accurate modeling, design, and load estimation of lcc-s based wpt system with a wide range of load," *IEEE Transactions on Power Electronics*, vol. 38, no. 10, pp. 11 763–11 775, 2023.

[43] K. Song, Z. Li, J. Jiang, and C. Zhu, "Constant current/voltage charging operation for series–series and series–parallel compensated wireless power transfer systems employing primary-side controller," *IEEE Transactions on Power Electronics*, vol. 33, no. 9, pp. 8065–8080, 2017.

[44] Z. Li, C. Zhu, J. Jiang, K. Song, and G. Wei, "A 3-kw wireless power transfer system for sightseeing car supercapacitor charge," *IEEE Transactions on Power Electronics*, vol. 32, no. 5, pp. 3301–3316, 2016.

[45] P. P. Mercier and A. P. Chandrakasan, "Rapid wireless capacitor charging using a multi-tapped inductively-coupled secondary coil," *IEEE Transactions on Circuits and Systems I: Regular Papers*, vol. 60, no. 9, pp. 2263–2272, 2013.

[46] W. Zhang, S.-C. Wong, K. T. Chi, and Q. Chen, "Analysis and comparison of secondary series-and parallel-compensated inductive power transfer systems operating for optimal efficiency and load-independent voltage-transfer ratio," *IEEE Transactions on Power Electronics*, vol. 29, no. 6, pp. 2979–2990, 2013.

[47] C.-S. Wang, G. A. Covic, and O. H. Stielau, "Power transfer capability and bifurcation phenomena of loosely coupled inductive power transfer systems," *IEEE transactions on industrial electronics*, vol. 51, no. 1, pp. 148–157, 2004.

[48] W. Zhang, S.-C. Wong, K. T. Chi, and Q. Chen, "Load-independent duality of current and voltage outputs of a series-or parallel-compensated inductive power transfer converter with optimized efficiency," *IEEE Journal of Emerging and Selected Topics in Power Electronics*, vol. 3, no. 1, pp. 137–146, 2014.

[49] W. Zhang and C. C. Mi, "Compensation topologies of high-power wireless power transfer systems," *IEEE Transactions on Vehicular Technology*, vol. 65, no. 6, pp. 4768–4778, 2015.

[50] X. Qu, Y. Jing, H. Han, S.-C. Wong, and K. T. Chi, "Higher order compensation for inductive-power-transfer converters with constant-voltage or constant-current output combating transformer parameter constraints," *IEEE Transactions on Power Electronics*, vol. 32, no. 1, pp. 394–405, 2016.

[51] F. Grazian, P. Van Duijsen, T. B. Soeiro, and P. Bauer, "Advantages and tuning of zero voltage switching in a wireless power transfer system," in *2019 IEEE PELS Workshop on Emerging Technologies: Wireless Power Transfer (WoW)*. IEEE, 2019, pp. 367–372.

[52] W. Zhong, D. Xu, and R. Y. Hui, "Wireless power transfer," in *Between Distance and Efficiency, Zhejiang University*. Springer, 2020.

[53] W. Zhang, S.-C. Wong, K. T. Chi, and Q. Chen, "Design for efficiency optimization and voltage controllability of series–series compensated inductive power transfer systems," *IEEE Transactions on Power Electronics*, vol. 29, no. 1, pp. 191–200, 2013.

[54] I. C. on Non-Ionizing Radiation Protection *et al.*, "Guidelines for limiting exposure to electromagnetic fields (100 khz to 300 ghz)," *Health physics*, vol. 118, no. 5, pp. 483–524, 2020.

[55] ——, "Guidelines for limiting exposure to time-varying electric and magnetic fields (1 hz to 100 khz)," *Health physics*, vol. 99, no. 6, pp. 818–836, 2010.

[56] e Magnetica, “Current loop magnetic field calculator,” 2024, accessed: 2024-08-27. [Online]. Available: https://www.e-magnetica.pl/doku.php/calculator/current_loop_axis

[57] T. Martinez, M. Almanza, Y. Civet, and Y. Perriard, “A cockcroft-walton generator driven by wireless power transfer for implanted high-voltage generation,” in *2021 24th International Conference on Electrical Machines and Systems (ICEMS)*. IEEE, 2021, pp. 243–246.

[58] S. Li, X. Yu, Y. Yuan, S. Lu, and T. Li, “A novel high-voltage power supply with mhz wpt techniques: Achieving high-efficiency, high-isolation, and high-power-density,” *IEEE Transactions on Power Electronics*, 2023.

[59] Y. Liang, P. Sun, X. Wu, L. Wang, J. Sun, E. Rong, and Q. Deng, “Input-series output-series (isos) multi-channel ipt system for high-voltage and high-power wireless power transfer,” *IEEE Journal of Emerging and Selected Topics in Power Electronics*, 2023.

[60] M. Leibl, O. Knecht, and J. W. Kolar, “Inductive power transfer efficiency limit of a flat half-filled disc coil pair,” *IEEE Transactions on Power Electronics*, vol. 33, no. 11, pp. 9154–9162, 2018.

[61] J. Liu, Q. Deng, D. Czarkowski, M. K. Kazimierczuk, H. Zhou, and W. Hu, “Frequency optimization for inductive power transfer based on ac resistance evaluation in litz-wire coil,” *IEEE Transactions on Power Electronics*, vol. 34, no. 3, pp. 2355–2363, 2018.

[62] H. Greinacher, “Über eine methode, wechselstrom mittels elektrischer ventile und kondensatoren in hochgespannten gleichstrom umzuwandeln,” *Zeitschrift für Physik*, vol. 4, no. 2, pp. 195–205, 1921.

[63] J. D. Cockcroft and E. T. Walton, “Experiments with high velocity positive ions.—(i) further developments in the method of obtaining high velocity positive ions,” *Proceedings of the royal society of London. Series A, containing papers of a mathematical and physical character*, vol. 136, no. 830, pp. 619–630, 1932.

[64] E. T. Walton, “Ernest T.S. Walton – Facts,” https://www.nobelprize.org/prizes/physics/1951/walton/facts/, Nobel Prize Outreach AB, 2024.

[65] E. Sato, E. Tanaka, H. Mori, T. Kawai, T. Ichimaru, S. Sato, K. Takayama, and H. Ido, “Demonstration of enhanced-edge angiography using a cerium target x-ray generator: Cerium target x-ray generator,” *Medical physics*, vol. 31, no. 11, pp. 3017–3021, 2004.

[66] S. Talukder, S. Park, and J. Rivas-Davila, “A portable electrostatic precipitator to reduce respiratory death in rural environments,” in *2017 IEEE 18th Workshop on Control and Modeling for Power Electronics (COMPEL)*. IEEE, 2017, pp. 1–7.

[67] A. Brunner, R. Crittenden, A. Dzierba, J. Gunter, R. Gardner, C. Hamm, R. Lindenbusch, D. Rust, E. Scott, P. Smith *et al.*, “A cockcroft–walton base for the feu84-3 photomultiplier tube,” *Nuclear Instruments and Methods in*

Physics Research Section A: Accelerators, Spectrometers, Detectors and Associated Equipment, vol. 414, no. 2-3, pp. 466–476, 1998.

[68] S. Fan, Z. Yuan, W. Gou, Y. Zhao, C. Song, Y. Huang, J. Zhou, and L. Geng, "A 2.45-ghz rectifier-booster regulator with impedance matching converters for wireless energy harvesting," *IEEE Transactions on Microwave Theory and Techniques*, vol. 67, no. 9, pp. 3833–3843, 2019.

[69] S. Park, D. S. Drew, S. Follmer, and J. Rivas-Davila, "Lightweight high voltage generator for untethered electroadhesive perching of micro air vehicles," *IEEE Robotics and Automation Letters*, vol. 5, no. 3, pp. 4485–4492, 2020.

[70] W. Shen, J. Peng, R. Ma, J. Wu, J. Li, Z. Liu, J. Leng, X. Yan, and M. Qi, "Sunlight-powered sustained flight of an ultralight micro aerial vehicle," *Nature*, vol. 631, no. 8021, pp. 537–543, 2024.

[71] S. Park, J. Yang, and J. Rivas-Davila, "A hybrid cockcroft–walton/dickson multiplier for high voltage generation," *IEEE Transactions on Power Electronics*, vol. 35, no. 3, pp. 2714–2723, 2019.

[72] J. Kuffel and P. Kuffel, *High voltage engineering fundamentals*. Elsevier, 2000.

[73] M. Abdel-Salam, *High-voltage engineering: theory and practice, revised and expanded*. CRC Press, 2018.

[74] I. C. Kobougias and E. C. Tatakis, "Optimal design of a half-wave cockcroft–walton voltage multiplier with minimum total capacitance," *IEEE transactions on Power Electronics*, vol. 25, no. 9, pp. 2460–2468, 2010.

[75] S. Mao, C. Li, W. Li, J. Popović, S. Schröder, and J. A. Ferreira, "Unified equivalent steady-state circuit model and comprehensive design of the lcc resonant converter for hv generation architectures," *IEEE Transactions on Power Electronics*, vol. 33, no. 9, pp. 7531–7544, 2017.

[76] S. Mao, J. Popović, and J. A. Ferreira, "Diode reverse recovery process and reduction of a half-wave series cockcroft–walton voltage multiplier for high-frequency high-voltage generator applications," *IEEE Transactions on Power Electronics*, vol. 34, no. 2, pp. 1492–1499, 2018.

[77] W. Qian, "Modeling and analysis of high frequency high voltage multiplier circuit for high voltage power supply," 2017.

[78] G. B. Joun and B. H. Cho, "An energy transmission system for an artificial heart using leakage inductance compensation of transcutaneous transformer," *IEEE Transactions on Power Electronics*, vol. 13, no. 6, pp. 1013–1022, 1998.

[79] Q. Chen, S. C. Wong, K. T. Chi, and X. Ruan, "Analysis, design, and control of a transcutaneous power regulator for artificial hearts," *IEEE Transactions on Biomedical Circuits and Systems*, vol. 3, no. 1, pp. 23–31, 2009.

[80] J. Hou, Q. Chen, Z. Zhang, S.-C. Wong, and K. T. Chi, "Analysis of output current characteristics for higher order primary compensation in inductive power transfer systems," *IEEE Transactions on Power Electronics*, vol. 33, no. 8, pp. 6807–6821, 2017.

[81] R. He, P. Zhao, M. Fu, Y. Liu, H. Wang, and J. Liang, "Decomposition and synthesis of high-order compensated inductive power transfer systems for improved output controllability," *IEEE Transactions on Microwave Theory and Techniques*, vol. 67, no. 11, pp. 4514–4523, 2019.

[82] S. Li, W. Li, J. Deng, T. D. Nguyen, and C. C. Mi, "A double-sided lcc compensation network and its tuning method for wireless power transfer," *IEEE transactions on Vehicular Technology*, vol. 64, no. 6, pp. 2261–2273, 2014.

[83] J. Feng, M. Fu, Q. Li, and F. C. Lee, "Resonant converter with coupling and load independent resonance for omnidirectional wireless power transfer application," in *2017 IEEE Energy Conversion Congress and Exposition (ECCE)*. IEEE, 2017, pp. 2596–2601.

[84] A. K. Bhat, "Fixed-frequency pwm series-parallel resonant converter," *IEEE Transactions on Industry Applications*, vol. 28, no. 5, pp. 1002–1009, 1992.

[85] Z. Li, H. Liu, Y. Tian, and Y. Liu, "Constant current/voltage charging for primary-side controlled wireless charging system without using dual-side communication," *IEEE Transactions on Power Electronics*, vol. 36, no. 12, pp. 13 562–13 577, 2021.

[86] G. Ivensky, A. Kats, and S. Ben-Yaakov, "An rc load model of parallel and series-parallel resonant dc-dc converters with capacitive output filter," *IEEE Transactions on Power Electronics*, vol. 14, no. 3, pp. 515–521, 1999.

[87] A. K. Rathore and V. R. Vakacharla, "A simple technique for fundamental harmonic approximation analysis in parallel and series–parallel resonant converters," *IEEE Transactions on Industrial Electronics*, vol. 67, no. 11, pp. 9963–9968, 2019.

[88] M. Qin, W. Chen, A. Ye, F. Zhang, S. M. Goetz, F. Yang, Z. Yu, and X. Yang, "Adaptive optimization charging strategy for lcc resonant capacitor charging power supply," *IEEE Journal of Emerging and Selected Topics in Power Electronics*, 2023.

[89] F. Xu, Y. Guo, and X. Zhang, "An enhanced quasi-cc output model of lcc-p compensated inductive-power-transfer converters," *IEEE Transactions on Power Electronics*, 2023.

[90] Y. Guo, L. Wang, Y. Zhang, S. Li, and C. Liao, "Rectifier load analysis for electric vehicle wireless charging system," *IEEE Transactions on Industrial Electronics*, vol. 65, no. 9, pp. 6970–6982, 2018.

[91] Y. Guo, Y. Zhang, W. Zhang, and L. Wang, "Battery parameter identification based on wireless power transfer system with rectifier load," *IEEE Transactions on Industrial Electronics*, vol. 68, no. 8, pp. 6893–6904, 2020.

[92] M. Fu, Z. Tang, and C. Ma, "Analysis and optimized design of compensation capacitors for a megahertz wpt system using full-bridge rectifier," *IEEE Transactions on Industrial Informatics*, vol. 15, no. 1, pp. 95–104, 2018.

[93] A. Namadmalan, J. M. Alonso, and A. Iqbal, "Accurate fundamental harmonic modeling of inductive power transfer battery chargers," *IEEE Transactions on Transportation Electrification*, vol. 8, no. 1, pp. 627–635, 2021.

[94] P. Zhang, X. Yu, Q. Yang, Z. Li, C. Cai, Z. Yuan, X. Zhang, H. Lin, H. Yang, and L. Liu, "Wireless power transfer-based voltage equalizer for scalable cell-string charging," *IEEE Transactions on Industrial Electronics*, vol. 71, no. 1, pp. 493–503, 2023.

[95] P. Zhang, X. Yu, X. Zhang, Q. Yang, Z. Li, Z. Yuan, C. Cai, H. Lin, H. Yang, and L. Liu, "Wireless charging of large-scale energy storage systems: A hybridized ad-hoc approach for high-efficiency," *IEEE Transactions on Power Electronics*, 2023.

[96] S. Yin, X. Xin, R. Wang, M. Dong, J. Lin, Y. Gu, and H. Li, "A 1-mhz gan-based $lclc$ resonant step-up converter with air-core transformer for satellite electric propulsion application," *IEEE Transactions on Industrial Electronics*, vol. 69, no. 11, pp. 11 035–11 045, 2021.

[97] S.-H. Son, T.-H. Kim, C.-H. Kwon, S.-R. Jang, C.-H. Yu, and H.-S. Kim, "Lumped parameter model of cockcroft-walton voltage multiplier in resonant converters," in *2023 11th International Conference on Power Electronics and ECCE Asia (ICPE 2023-ECCE Asia)*. IEEE, 2023, pp. 2681–2687.

[98] S.-H. Son, J.-S. Bae, T.-H. Kim, C.-H. Gwon, S.-R. Jang, C.-H. Yu, and H.-S. Kim, "Development of 80-kw high-voltage power supply for x-ray generator," *IEEE Transactions on Industrial Electronics*, vol. 70, no. 4, pp. 3652–3662, 2022.

[99] J. Gao, Q. Chen, X. Ren, Z. Zhang, H. Shi, and H. Ran, "Design and analysis of the s/p compensated contactless converter for high voltage ignition," in *2018 IEEE Applied Power Electronics Conference and Exposition (APEC)*. IEEE, 2018, pp. 1080–1085.

[100] S. Zhou, Q. Chen, B. Zhang, J. Gao, K. T. Chi, and L. Xu, "Effects of nonlinear junction capacitance of rectifiers on performance of high voltage power supplies," *IEEE Transactions on Power Electronics*, 2023.

[101] Z. Huang, C.-S. Lam, P.-I. Mak, R. P. da Silva Martins, S.-C. Wong, and K. T. Chi, "A single-stage inductive-power-transfer converter for constant-power and maximum-efficiency battery charging," *IEEE Transactions on Power Electronics*, vol. 35, no. 9, pp. 8973–8984, 2020.

[102] Z. Huang, S.-C. Wong, and K. T. Chi, "An inductive-power-transfer converter with high efficiency throughout battery-charging process," *IEEE Transactions on Power Electronics*, vol. 34, no. 10, pp. 10 245–10 255, 2019.

[103] Z. Li, K. Song, J. Jiang, and C. Zhu, “Constant current charging and maximum efficiency tracking control scheme for supercapacitor wireless charging,” *IEEE Transactions on Power Electronics*, vol. 33, no. 10, pp. 9088–9100, 2018.

[104] M. Fu, T. Zhang, C. Ma, and X. Zhu, “Efficiency and optimal loads analysis for multiple-receiver wireless power transfer systems,” *IEEE Transactions on Microwave Theory and Techniques*, vol. 63, no. 3, pp. 801–812, 2015.

[105] M. Fu, T. Zhang, X. Zhu, P. C.-K. Luk, and C. Ma, “Compensation of cross coupling in multiple-receiver wireless power transfer systems,” *IEEE Transactions on Industrial Informatics*, vol. 12, no. 2, pp. 474–482, 2016.